

## Chapter 2

# Towards Strongly Interacting Bosons and Fermions

This chapter sets the stage from which this thesis departs into the realm of strongly interacting bosons and fermions. Several theoretical concepts that are needed for a basic understanding of the experiments in later chapters are briefly summarized.

The first section introduces theoretical background on ultracold quantum gases. After a fast journey through second quantization, quantum statistics and basics of statistical mechanics, ideal fermions and weakly interacting bosons are discussed in the Thomas-Fermi limit. The consequences of interactions in ultracold quantum gases are exemplarily illustrated in a mean-field analysis of an interacting Bose-Fermi mixture in a harmonic trap. The section concludes with a discussion of possible routes towards strongly interacting quantum systems. The second section is dedicated to the theory of optical lattices. After discussing the landscape of experimental lattice potentials, we turn to the band structure of a simple cubic lattice and introduce the Wannier basis. In the third section, the concept of Feshbach resonances is presented. After a brief summary of the basics of quantum mechanical scattering theory, resonance scattering, the emergence of bound molecular states and the problem of two interacting atoms in a tight harmonic potential are discussed. Finally, the specific Feshbach resonances that are used in the experiments of this thesis are introduced.

## 2.1 Ultracold Quantum Gases

We start with a reminder of quantum statistics [1] and many-body quantum theory in second quantization [2]. Second quantization is the language of choice to formulate the many-body Hamiltonians for bosons and fermions in optical lattice potentials. It is heavily used throughout the thesis. Then, basic formalisms for bosonic and fermionic quantum gases in harmonic trapping potentials are introduced, including the important Thomas-Fermi approximation [3–5]. The bosonic and fermionic formalisms are both applied in a self-consistent mean-field calculation for an interacting Bose-Fermi mixture in a harmonic trap, revealing a marked influence of inter-species interactions on the phases of the mixture. Finally, we discuss under which

conditions a quantum system can be regarded as strongly interacting [6, 7] and identify fundamental routes to reach this regime with ultracold atoms.

### 2.1.1 Bosons and Fermions

Indistinguishability of particles is a fundamental concept of quantum theory. We consider a system of  $N$  indistinguishable particles. The single-particle states in the system are described by a basis of single-particle wavefunctions  $\{\psi_E(x)\}$ , where  $x$  denotes the collection of spatial and spin coordinates and  $E$  uniquely labels the state by representing a complete set of single-particle quantum numbers. For example, for free fermions in a box  $E$  denotes the momentum  $\mathbf{k}$  and the  $z$ -component of the spin,  $s_z$ . Using the single-particle wavefunctions, the most general many-particle wavefunction  $\Psi(x_1, \dots, x_N)$  for the whole  $N$ -particle system can be constructed by

$$\Psi(x_1, \dots, x_N) = \sum_{E_1, \dots, E_N} C(E_1, \dots, E_N) \psi_{E_1}(x_1) \cdots \psi_{E_N}(x_N), \quad (2.1)$$

where each  $E_k$  in the sum runs over the complete set of quantum numbers. Because quantum particles are fundamentally indistinguishable, a single-particle wavefunction cannot be strictly assigned to a certain particle. This implies the invariance of observables under the exchange of particles. Particularly, the probability density  $|\Psi|^2$  must be unchanged:

$$|\Psi(\dots, x_k, \dots, x_l, \dots)|^2 = |\Psi(\dots, x_l, \dots, x_k, \dots)|^2. \quad (2.2)$$

From this we conclude that there are two possibilities for the sign of the many-particle wavefunction when particle coordinates are exchanged:

$$\Psi(\dots, x_k, \dots, x_l, \dots) = \pm \Psi(\dots, x_l, \dots, x_k, \dots). \quad (2.3)$$

Therefore, the principle of indistinguishability suggests that quantum particles are grouped into two fundamental classes: First, the bosons, for which the wavefunction transforms symmetrically (upper sign). Second, the fermions, for which the wavefunction transforms antisymmetrically (lower sign). Indeed, the famous spin-statistics theorem in quantum field theory states, that particles with integer spin are bosons and particles with half-integer spin are fermions [8]. According to Eq. 2.3 two fermions cannot occupy the same quantum state, because then  $\Psi$  would be equal to  $-\Psi$  implying, that the wavefunction must vanish

$$\Psi(\dots, x_k, \dots, x_k, \dots) = 0. \quad (2.4)$$

This is Pauli's exclusion principle for fermions.

Quantum statistics has a profound impact on the construction of many-particle wavefunctions. For the case of bosons, a single-particle quantum state can be occupied by many particles. Accordingly, the general many-particle wavefunction for  $N$  bosons is expanded in terms of a basis of completely symmetrized wavefunctions

$$\Phi_{n_1, \dots, n_\infty}^B(x_1, \dots, x_N) = \left( \frac{n_1! \cdots n_\infty!}{N!} \right)^{1/2} \sum_{\substack{E_1, \dots, E_N \\ (n_1, \dots, n_\infty)}} \psi_{E_1}(x_1) \cdots \psi_{E_N}(x_N). \quad (2.5)$$

Here, the sum runs over all possibilities, in which  $N$  particles are distributed over the single-particle states, such that  $n_1$  particles are in state  $\psi_{E_1}$ ,  $n_2$  particles are in state  $\psi_{E_2}$  and so on. In total, there are  $N!/(n_1! n_2! \cdots n_\infty!)$  possibilities, which explains the normalization.

In the case of fermions, Pauli's principle restricts the occupation of single-particle states to either  $n_k = 0$  or 1. The basis states of the general many-particle wavefunction for  $N$  fermions are given by the normalized Slater determinants

$$\Phi_{n_1, \dots, n_\infty}^F(x_1, \dots, x_N) = \frac{1}{\sqrt{N!}} \begin{vmatrix} \psi_{E_1}(x_1) & \psi_{E_1}(x_2) & \cdots & \psi_{E_1}(x_N) \\ \psi_{E_2}(x_1) & \psi_{E_2}(x_2) & \cdots & \psi_{E_2}(x_N) \\ \vdots & \vdots & \ddots & \vdots \\ \psi_{E_N}(x_1) & \psi_{E_N}(x_2) & \cdots & \psi_{E_N}(x_N) \end{vmatrix}. \quad (2.6)$$

The mathematical properties of the determinant ensure, that the basis wavefunctions transform antisymmetrically under exchange of any two particles.

## Second Quantization

Second quantization offers a convenient way to capture the symmetry properties of bosons and fermions without explicitly writing down the above many-particle basis states during calculations. The underlying formalism implicitly takes care of maintaining the appropriate symmetry of the many-particle wavefunctions. For example the completely symmetrized bosonic  $N$ -particle state 2.5 is represented by an occupation number state  $|\Phi_{n_1, \dots, n_\infty}^B\rangle = |n_1, n_2, \dots\rangle \equiv |n_1\rangle|n_2\rangle \cdots |n_\infty\rangle$  with the occupation numbers  $n_i$  as defined above.

For bosons, the whole range of integer occupation numbers is allowed, including zero. In order to construct and manipulate the occupation number states, the creation and annihilation operators  $\hat{a}_k^\dagger$  and  $\hat{a}_k$  are introduced for each single-particle state  $k$ . The operators obey the bosonic commutation relations

$$[\hat{a}_k, \hat{a}_l]_- = 0, \quad [\hat{a}_k^\dagger, \hat{a}_l^\dagger]_- = 0 \quad \text{and} \quad [\hat{a}_k, \hat{a}_l^\dagger]_- = \delta_{kl}, \quad (2.7)$$

where  $[A, B]_- = AB - BA$ . These relations determine all properties of the operators. They imply, that the creation operator  $\hat{a}_k^\dagger$  raises and the annihilation operator  $\hat{a}_k$

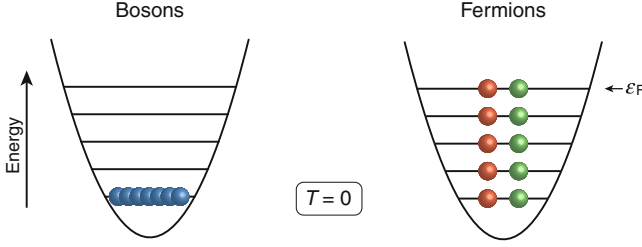


**Fig. 2.1** Bosonic and fermionic quantum statistics. At zero temperature bosons form a Bose-Einstein condensate, while fermions arrange in a Fermi sea. The energy of the highest occupied state in the Fermi sea is the Fermi energy  $\epsilon_F$ . Green and red balls correspond to two spin states (spin up and spin down). The color coding introduced in this figure is kept throughout the thesis: blue balls indicate bosons, red and green balls indicate fermions

lowers the number of particles in the single-particle state  $\psi_{E_k}$  by one according to  $\hat{a}_k^\dagger |n_k\rangle = \sqrt{n_k + 1} |n_k + 1\rangle$ ,  $\hat{a}_k |n_k\rangle = \sqrt{n_k} |n_k - 1\rangle$ , and especially  $\hat{a}_k |0\rangle = 0$ , where  $|0\rangle$  is the vacuum state. Furthermore, it is easy to show that the eigenvalues of the operator  $\hat{n}_k \equiv \hat{a}_k^\dagger \hat{a}_k$  correspond to the number of particles occupying the single-particle state  $\psi_{E_k}$ , which suggests the name number operator for  $\hat{n}_k$ .

For fermions, the occupation numbers are restricted to  $n_k = 0$  or 1 and the many-particle wavefunction must be antisymmetric. Those requirements are automatically taken care of by defining the anticommutation relations for the fermionic creation and annihilation operators  $c_k^\dagger$  and  $c_k$  according to

$$[\hat{c}_k, \hat{c}_l]_+ = 0, \quad [\hat{c}_k^\dagger, \hat{c}_l^\dagger]_+ = 0 \quad \text{and} \quad [\hat{c}_k, \hat{c}_l^\dagger]_+ = \delta_{kl}, \quad (2.8)$$

where  $[A, B]_+ = AB + BA$ . With these relations one can show, that  $\hat{c}_k^\dagger \hat{c}_k^\dagger |0\rangle = 0$ , which prevents double occupation of a single quantum state (Pauli's exclusion principle), as well as  $c_k^\dagger |0\rangle = |1\rangle$ ,  $c_k^\dagger |1\rangle = 0$ ,  $c_k |1\rangle = |0\rangle$  and  $c_k |0\rangle = 0$ .

Within the formalism of second quantization it is simple to write down many-particle ground states. For  $N$  noninteracting, spinless bosons with the single-particle ground state  $\psi_{E_0}$ , the many-particle ground state can be directly constructed via

$$|\Phi_B\rangle = |N, 0, 0, \dots\rangle \equiv \frac{1}{\sqrt{N!}} (\hat{a}_0^\dagger)^N |0, 0, 0, \dots\rangle. \quad (2.9)$$

In this state, all particles occupy the same single-particle state, which is the defining property of a Bose-Einstein condensate (see Fig. 2.1).

In a fermionic  $N$ -particle system each single-particle state can only be occupied by a single fermion at most. Therefore, the zero-temperature many-particle ground state is realized, when the  $N$  single-particle states with lowest energy are filled from bottom up as expressed by

$$|\Phi_F\rangle = |\underbrace{1, 1, \dots, 1}_{N \text{ times}}, 0, 0, \dots, 0\rangle = \prod_{k \leq k_F} \hat{c}_k^\dagger |0, 0, 0, \dots\rangle. \quad (2.10)$$

The indices are ordered in such a way, that a lower index corresponds to a lower energy. The index  $k_F$  is defined such, that  $\sum_{k \leq k_F} = N$ . The energy  $E_{k_F} \equiv \epsilon_F$  of the highest occupied single-particle state is called the Fermi energy (see Fig. 2.1).

## Operators in Second Quantization

As shown above, second quantization offers a concise way to express many-particle states. However, the formalism unfolds its full potential, when it is used to rewrite  $N$ -particle Hamiltonians in a way that allows for elegant diagonalization formalisms. In real space, a  $N$ -particle Hamiltonian generally has the form

$$\begin{aligned} H = & \sum_{k=1}^N T(x_k) + \sum_{k \neq l=1}^N V_2(x_k, x_l) \\ & + \sum_{k \neq l \neq m=1}^N V_3(x_k, x_l, x_m) + \dots \end{aligned} \quad (2.11)$$

Here  $T(x_k)$  denotes an operator acting on a single particle (e.g. kinetic or potential energy),  $V_2(x_k, x_l)$  an operator acting on two particles (e.g. two-body interaction between particles) and  $V_3(x_k, x_l, x_m)$  an operator acting on three particles (e.g. three-body interaction between particles). Generally, also operators involving a larger number of particles can play a role as indicated by the dots. We will see in Chap. 7 that higher particle terms can happen to be relevant not only theoretically, but also experimentally. In second quantization the Hamiltonian takes the form [2]

$$\begin{aligned} \hat{H} = & \sum_{ij} \hat{a}_i^\dagger \langle i|T|j\rangle \hat{a}_j + \frac{1}{2} \sum_{ijkl} \hat{a}_i^\dagger \hat{a}_j^\dagger \langle ij|V_2|kl\rangle \hat{a}_l \hat{a}_k \\ & + \frac{1}{6} \sum_{ijk} \hat{a}_i^\dagger \hat{a}_j^\dagger \hat{a}_k^\dagger \langle ijk|V_3|lmn\rangle \hat{a}_n \hat{a}_m \hat{a}_l + \dots \end{aligned} \quad (2.12)$$

Here, only the case of bosonic operators is shown for brevity. The identical expression holds for fermions, when the operators  $\hat{a}_k$  are replaced by  $\hat{c}_k$ . However, it is very important to keep the ordering of the indices as changes affect the overall sign. The matrix elements are complex numbers that are calculated by integration over the generalized coordinate  $x$ , for example  $\langle i|T|j\rangle = \int dx \psi_{E_i}^*(x) T(x) \psi_{E_j}(x)$ . We come across Hamiltonians of this kind several times in this thesis. Nevertheless, it is often convenient to use Hamiltonian 2.12 in a slightly different form that is obtained by introducing the field operators  $\hat{\psi}(x) = \sum_k \psi_k(x) \hat{a}_k$  and  $\hat{\psi}^\dagger(x) = \sum_k \psi_k^*(x) \hat{a}_k^\dagger$ .

A simple calculation yields

$$\begin{aligned} \hat{H} = & \int dx \hat{\psi}^\dagger(x) T(x) \hat{\psi}(x) + \frac{1}{2} \int dx dx' \hat{\psi}^\dagger(x) \hat{\psi}^\dagger(x') V_2(x, x') \hat{\psi}(x') \hat{\psi}(x) \\ & + \frac{1}{6} \int dx dx' dx'' \hat{\psi}^\dagger(x) \hat{\psi}^\dagger(x') \hat{\psi}^\dagger(x'') V_3(x, x', x'') \hat{\psi}(x'') \hat{\psi}(x') \hat{\psi}(x) + \dots \end{aligned} \quad (2.13)$$

### 2.1.2 Bose-Einstein and Fermi-Dirac Distribution

In the preceding section, we have derived the effects of quantum statistics on an elementary level. However, in systems of practical importance the particle number is often very large and, even more importantly, such systems generally have a finite temperature. Therefore it is crucial to consider the impact of quantum statistics on statistical mechanics and thermodynamics.

According to the fundamental postulate of statistical mechanics, a macroscopic system in thermodynamic equilibrium is equally likely to be in any of the states that satisfy the macroscopic conditions [1]. This means, that the system is a member of an ensemble, in which the total energy  $E$ , the particle number  $N$  and the volume  $V$  are fixed. It is called the *microcanonical ensemble*. Remarkably, those conditions are quite closely met in experiments with ultracold atoms.<sup>1</sup> However, for calculations it is often more practical to consider the system being in contact with a large reservoir, which allows for the exchange of particles and energy. The corresponding ensemble is called the *grand canonical ensemble*, in which the temperature  $T = 1/(k_B \beta)$  and the chemical potential  $\mu$ , which is the energy cost to add a particle, are fixed. The probability of the system to be in any state with particle number  $N$  and total energy  $E$  is determined by the Boltzmann factor  $e^{-\beta(E - \mu N)}/Z$ , where  $Z$  is the partition function, which we are going to derive for ideal gases in the following. The partition function has crucial importance for the calculation of ensemble averages of physical observables (Fig. 2.2).

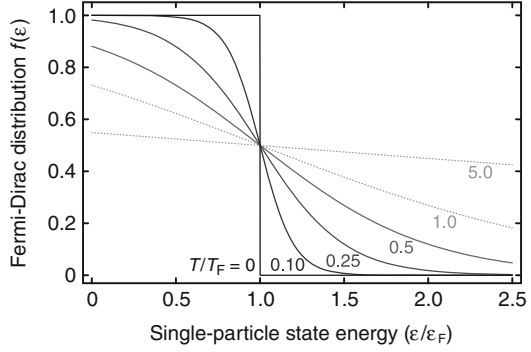
We assume an ideal gas consisting of noninteracting particles, where the eigenenergies of the single-particle states are denoted by  $\epsilon_i$  and the many-particle states are given by  $|n_1, \dots, n_\infty\rangle$  with the total energy  $\sum_i \epsilon_i n_i$ . The grand canonical partition function is then given by [2]

$$Z = \prod_{i=1}^{\infty} \text{Tr}_i e^{-\beta(\epsilon_i - \mu)\hat{n}_i} = \prod_{i=1}^{\infty} \sum_n \left( e^{-\beta(\epsilon_i - \mu)} \right)^n. \quad (2.14)$$

---

<sup>1</sup> This is true under the assumption that ultracold atom systems are truly in thermodynamic equilibrium. In practice, an ultracold sample under investigation has typically undergone a sequence of parameter changes, which can only be adiabatic to a certain degree. For example, changes of  $E$  and  $V$  are induced by variation of the interparticle interactions or the trapping potential.

**Fig. 2.2** Fermi-Dirac distribution for several dimensionless temperatures  $T/T_F$  as a function of the dimensionless energy of single-particle quantum states  $\epsilon/\epsilon_F$ . *Solid curves indicate the quantum degenerate regime*



We can further evaluate this expression by taking into account quantum statistics. For bosons, the occupation numbers  $n$  are unrestricted and cover all integer numbers, which yields

$$Z_B = \prod_i \frac{1}{1 - e^{-\beta(\epsilon_i - \mu)}} \quad (2.15)$$

and for fermions,  $n$  can either take the value 0 or 1, such that

$$Z_F = \prod_i (1 + e^{-\beta(\epsilon_i - \mu)}). \quad (2.16)$$

Now, statistics can be connected to thermodynamics via the fundamental relation [2]

$$\Omega(T, V, \mu) = -\frac{1}{\beta} \ln Z = \pm \frac{1}{\beta} \sum_i \ln(1 \mp e^{\beta(\mu - \epsilon_i)}), \quad (2.17)$$

which is the grand canonical potential that allows to calculate all macroscopic thermodynamic properties in equilibrium. The upper (lower) sign refers to bosons (fermions) in this and the following equations. The mean total atom number of the ideal gas is given by

$$\langle N \rangle = -\frac{\partial \Omega}{\partial \mu} = \sum_i \langle n_i \rangle \quad \text{with} \quad \langle n_i \rangle = \frac{1}{e^{\beta(\epsilon_i - \mu)} \mp 1} = f_{B/F}(\epsilon_i), \quad (2.18)$$

which are the famous Bose-Einstein and the Fermi-Dirac distributions for the mean occupation of individual quantum states in noninteracting systems. Additionally the mean entropy is given by [1]

$$\langle S \rangle = -\frac{\partial \Omega}{\partial T} = k_B \sum_i \frac{\beta(\epsilon_i - \mu)}{e^{\beta(\epsilon_i - \mu)} \mp 1} \mp k_B \ln \left( 1 \mp e^{-\beta(\epsilon_i - \mu)} \right) \quad (2.19)$$

It is important to note that the results derived here are generally valid for all systems of noninteracting bosonic and fermionic particles. However, for practical calculations it often proves useful to replace the discrete summations over the state index  $i$ , which appears in Eqs. 2.17–2.19, by a continuous integral. This leads to the concept of the density-of-states capturing the effects of the trapping potential on the energy levels.

### 2.1.3 Quantum Degenerate Fermionic Gases

A gas of fermionic atoms in a single spin state at low temperature is the “most ideal” gas one can think of. As we will discuss later in this chapter, low energy collisions between fermionic atoms are largely suppressed due to Pauli’s principle (see Sect. 2.3). We consider the gas to be trapped in a three-dimensional harmonic potential

$$V(\mathbf{r}) = \frac{1}{2}m \left( \omega_x^2 x^2 + \omega_y^2 y^2 + \omega_z^2 z^2 \right), \quad (2.20)$$

where  $m$  is the mass of the particles and the  $\omega_\alpha$  denote the trapping frequencies in each direction  $\alpha = x, y, z$ . The eigenenergies of the single-particle states are given by [9]

$$\epsilon_{n_x, n_y, n_z} = \hbar \sum_{\alpha} \omega_{\alpha} \left( n_{\alpha} + \frac{1}{2} \right). \quad (2.21)$$

This single-particle spectrum of the harmonic oscillator gives rise to the density-of-states<sup>2</sup>

$$g(\epsilon) = \frac{\epsilon^2}{2(\hbar\bar{\omega})^3}, \quad (2.22)$$

where  $\bar{\omega} = (\omega_x \omega_y \omega_z)^{1/3}$  is the geometric mean of the trapping frequencies. With Eq. 2.22 and the Fermi-Dirac distribution the total particle number  $N$  in the system can be expressed by

$$N = \int_0^\infty d\epsilon \frac{g(\epsilon)}{e^{\beta(\epsilon-\mu)} + 1} = - \left( \frac{k_B T}{\hbar\bar{\omega}} \right)^3 \text{Li}_3(-e^{\beta\mu}) \xrightarrow{\beta \rightarrow \infty} \int_0^\infty d\epsilon g(\epsilon) \Theta(\mu - \epsilon). \quad (2.23)$$

At a certain temperature  $T$  and total particle number  $N$ , this relation implicitly fixes the chemical potential  $\mu$ . When the temperature approaches zero, the Fermi-Dirac distribution becomes a step function, indicating that the single-particle states are filled from bottom up.<sup>3</sup> Under these conditions the chemical potential is called the

<sup>2</sup> The continuum approximation of the quantum mechanically discrete eigenenergies is strictly speaking only valid, when the discreteness is not resolved, for example, due to finite temperature. For the harmonic oscillator, the condition justifying the use of a density-of-states requires that  $k_B T \gg \hbar\omega_\alpha$  ( $\alpha = x, y, z$ ).

<sup>3</sup>  $\Theta(x)$  is defined as 0 for  $x < 0$  and 1 for  $x \geq 0$ .



Fermi energy  $\epsilon_F$ , denoting the energy of the highest occupied single-particle state. Using Eq. 2.23 we obtain

$$\epsilon_F = \hbar\bar{\omega}(6N)^{1/3}, \quad (2.24)$$

which allows for the definition of the Fermi temperature  $T_F = \epsilon_F/k_B$  and the Fermi momentum  $k_F = \sqrt{2m\epsilon_F/\hbar^2}$ . Furthermore, using the Eqs. 2.19 and 2.22 the total entropy of the system can be calculated [10, 11], which to the lowest order in the temperature reads

$$\frac{S}{k_B} = \pi^2 N \frac{T}{T_F} + \mathcal{O}\left[\left(\frac{T}{T_F}\right)^2\right]. \quad (2.25)$$

### Thomas-Fermi Approximation

The calculation of finite temperature properties of an ideal Fermi gas, such as the real space density distribution, is considerably simplified by taking a semi-classical approach that is called the Thomas-Fermi approximation. This approach is quantum in so far, that the Fermi-Dirac distribution is used, but classical in so far, that the energies of the single-particle states  $\epsilon$  are approximated by the classical Hamiltonian  $H(\mathbf{r}, \mathbf{p})$ , according to

$$f_F(\mathbf{r}, \mathbf{p}) = \frac{1}{e^{\beta\left(\frac{\mathbf{p}^2}{2m} + V(\mathbf{r}) - \mu\right)} + 1}. \quad (2.26)$$

The semi-classical approach is valid in the limit of large particle numbers and corresponds to a local-density approximation [5]. The volume of a single quantum state viewed in the classical phase space  $(\mathbf{r}, \mathbf{p})$  is  $(2\pi\hbar)^3$ . Accordingly, the real-space density distribution in an arbitrary potential  $V(\mathbf{r})$  is obtained by integration over all momenta [4, 5]

$$n_F(\mathbf{r}) = \frac{1}{(2\pi\hbar)^3} \int d\mathbf{p} f_F(\mathbf{r}, \mathbf{p}) = -\frac{1}{\lambda_{\text{dB}}^3} \text{Li}_{3/2}\left(-e^{\beta(\mu - V(\mathbf{r}))}\right), \quad (2.27)$$

where  $\lambda_{\text{dB}} = \sqrt{2\pi\hbar^2/mk_B T}$  is the de Broglie wavelength.  $\text{Li}_n(z)$  denotes the polylogarithm of  $n$ th order.<sup>4</sup>

---

<sup>4</sup> The polylogarithm is defined by a series expansion  $\text{Li}_n(z) = \sum_{k=1}^{\infty} z^k/k^n$  that can also be written as [4]

$$\text{Li}_n(z) = \frac{1}{\pi^n} \int d^{2n}r \frac{1}{e^{\mathbf{r}^2/z} - 1},$$

where  $\mathbf{r}$  denotes a vector in  $2n$  dimensions. Note the limiting values  $\text{Li}_n(z) \xrightarrow{z \ll 1} z$  and  $-\text{Li}_n(-z) \xrightarrow{z \rightarrow \infty} \ln^n(z)/\Gamma(n+1)$ , where  $\Gamma(n)$  is the Gamma function.

Assuming a three-dimensional harmonic potential  $V(\mathbf{r})$  (see Eq. 2.20), it is instructive to consider the Thomas-Fermi approximation in the limits of high and zero temperature. In the first case,  $T \rightarrow \infty$ , the classical Boltzmann distribution is recovered

$$n_{\text{cl}}(\mathbf{r}) = \frac{N}{\pi^{3/2} \sigma_x \sigma_y \sigma_z} e^{-\sum_{\alpha} \alpha^2 / \sigma_{\alpha}^2} \quad \text{with} \quad \sigma_{\alpha}^2 = \frac{k_B T}{m \omega_{\alpha}^2}, \quad (2.28)$$

corresponding to a Gaussian distribution as expected for a harmonic potential ( $\alpha = x, y, z$ ). In the second case,  $T \rightarrow 0$ , we obtain the profile

$$\begin{aligned} n_{\text{F}}(\mathbf{r}) &= \frac{(2m)^{3/2}}{6\pi^2 \hbar^3} \Re \left[ (\epsilon_{\text{F}} - V(\mathbf{r}))^{3/2} \right] \\ &= \frac{8}{\pi^2} \frac{N}{R_{\text{Fx}} R_{\text{Fy}} R_{\text{Fz}}} \Re \left[ \left( 1 - \sum_{\alpha} \frac{\alpha^2}{R_{\text{F}\alpha}^2} \right)^{3/2} \right], \end{aligned} \quad (2.29)$$

keeping in mind the definition of the Fermi energy  $\epsilon_{\text{F}}$  as the zero temperature chemical potential 2.24. The extension of the cloud in the directions of the harmonic potential that is possible at the energy  $\epsilon_{\text{F}}$  is called the Fermi radius

$$R_{\text{F}\alpha} = \sqrt{\frac{2\epsilon_{\text{F}}}{m\omega_{\alpha}^2}} = \sqrt{\frac{\hbar}{m\omega_{\alpha}}} (48N)^{1/6}. \quad (2.30)$$

The density profiles  $n_{\text{cl}}(\mathbf{r})$  and  $n_{\text{F}}(\mathbf{r})$  play an important role in the thermometry of ultracold fermion clouds, which is discussed in Chap. 6 and Appendix C.

### 2.1.4 Quantum Degenerate Bosonic Gases

The behavior of an ideal gas of bosonic atoms differs fundamentally from the fermionic case: When the temperature is lowered, an ideal Bose gas undergoes a phase transition and the single-particle ground state of the system becomes macroscopically occupied. This phenomenon of Bose-Einstein condensation is fundamentally rooted in quantum statistics and can be identified on general grounds by examining the Bose-Einstein distribution (see Eq. 2.18)

$$f_{\text{B}}(\epsilon_i) = \frac{1}{e^{\beta(\epsilon_i - \mu)} - 1}. \quad (2.31)$$

Assuming without loss of generality, that the energy of the single-particle ground state  $\epsilon_0$  vanishes,  $f_{\text{B}}(\epsilon_0) \xrightarrow{\beta \rightarrow \infty} \infty$  diverges, when the temperature approaches zero. Note that  $\mu \leq 0$ , because  $f_{\text{B}}(\epsilon_i)$  must assume nonnegative values. The divergence of

the Bose-Einstein distribution entails a macroscopic occupation of the single-particle ground state.

Assuming a three-dimensional harmonic oscillator with the density-of-states 2.22, we obtain for the total particle number

$$N - N_0 = \int_0^\infty d\epsilon \frac{g(\epsilon)}{e^{\beta(\epsilon-\mu)} - 1} = \left( \frac{k_B T}{\hbar \bar{\omega}} \right)^3 \text{Li}_3(e^{\beta\mu}) \quad (2.32)$$

where it is crucial to separate out the ground state occupation  $N_0$  that is otherwise not properly accounted for by the integral. The maximal particle number that could be accommodated in the system at a fixed temperature without condensation,  $N_0 = 0$ , is reached for  $e^{\beta\mu} \rightarrow 1$  since  $\text{Li}_3(z)$  is monotonically increasing and  $0 \leq e^{\beta\mu} \leq 1$ . Therefore, the chemical potential must be  $\mu = 0$  at this point. In turn, if a fixed number of particles is to be accommodated in the system, there is a critical temperature  $T_c$ , below which a fraction of the atoms must occupy the ground state. The critical temperature follows from Eq. 2.32 by setting  $N_0 = 0$  and  $\mu = 0$

$$k_B T_c = \hbar \bar{\omega} \left( \frac{N}{\text{Li}_3(1)} \right)^{1/3} \approx 0.94 \hbar \bar{\omega} N^{1/3}. \quad (2.33)$$

Insertion of this result into Eq. 2.32 yields the fraction of condensed atoms as a function of temperature

$$\frac{N_0}{N} = 1 - \left( \frac{T}{T_c} \right)^3. \quad (2.34)$$

Using a semi-classical approach analogous to Eq. 2.27, it turns out that condensation sets in, when the density reaches  $n_B^{\text{max}} = \text{Li}_{3/2}(1)/\lambda_{\text{dB}}^3 = 2.612/\lambda_{\text{dB}}^3$ . This corresponds to the intuitive argument that Bose-Einstein condensation happens, when the de Broglie wavelength reaches the same order of magnitude as the interparticle spacing.

### Weakly Interacting Bose Gas

Atomic Bose gases are not as ideal as spin-polarized Fermi gases, because interactions are not suppressed at low temperatures. A realistic description needs to include interparticle interactions and this has been successfully done using the Gross-Pitaevskii Eq. (2.3) for the ground state of the many-particle system  $\Phi(\mathbf{r}, t)$ . This is a nonlinear Schrödinger equation

$$i \hbar \frac{\partial}{\partial t} \Phi(\mathbf{r}, t) = \left( -\frac{\hbar^2}{2m} \Delta + V(\mathbf{r}) + g |\Phi(\mathbf{r}, t)|^2 \right) \Phi(\mathbf{r}, t), \quad (2.35)$$

where the interactions are included by the parameter  $g = 4\pi\hbar^2 a_s/m$  with the scattering length  $a_s$  (see Sect. 2.3 for further details). With the knowledge, that in a pure Bose-Einstein condensate all atoms occupy an unique single-particle state, it is plausible to make the ansatz  $\Phi(\mathbf{r}, t) = \phi(\mathbf{r})e^{-i\mu t/\hbar}$ . Here,  $\phi(\mathbf{r})$  is understood to be normalized to the total particle number  $\int d\mathbf{r} |\phi(\mathbf{r})|^2 = N$  and  $\mu$  is the chemical potential. Accordingly, the time independent Gross-Pitaevskii equation reads

$$\left(-\frac{\hbar^2}{2m}\Delta + V(\mathbf{r}) + g|\phi(\mathbf{r})|^2\right)\phi(\mathbf{r}) = \mu\phi(\mathbf{r}), \quad (2.36)$$

allowing to calculate the real space wavefunction  $\phi(\mathbf{r})$  that is connected to the density distribution via  $n_B(\mathbf{r}) = |\phi(\mathbf{r})|^2$ . In general, this equation must be solved numerically. However, it turns out that under most experimental conditions the contribution of the kinetic energy term, proportional to  $\Delta$ , is negligible compared to the potential and interaction energy [3]. Omitting the kinetic energy, the real space density of the weakly interacting Bose gas is simply given by

$$n_B(\mathbf{r}) = |\psi(\mathbf{r})|^2 = \max\left[\frac{\mu - V(\mathbf{r})}{g}, 0\right]. \quad (2.37)$$

This approximation is also called Thomas-Fermi approximation due to the close analogy to Eq. 2.29.

For the case of harmonic confinement (Eq. 2.20), it is straightforward to derive for the chemical potential

$$\mu = \frac{\hbar\bar{\omega}}{2} \left(\frac{15Na_s}{\ell}\right)^{2/5}, \quad (2.38)$$

where  $\ell = \sqrt{\hbar/(m\bar{\omega})}$  is the harmonic oscillator length corresponding to  $\bar{\omega}$ . The Thomas-Fermi radius for weakly interacting bosons in a spherically symmetric trap is given by

$$R_B = \ell \left(\frac{15Na_s}{\ell}\right)^{1/5}. \quad (2.39)$$

### 2.1.5 Interacting Bose-Fermi Mixtures in a Harmonic Trap

In the experiment, we realize interacting mixtures of quantum degenerate bosons and fermions by sympathetic cooling in a harmonic trap. This technique requires both interactions and good overlap of the two species to ensure proper thermalization. However, when approaching the quantum degenerate regime, the densities can become high enough that interactions considerably influence the density distribution of both species inside the trap. In the case of repulsive interactions they can even phase separate.

In the following section, we will derive phases of a quantum degenerate interacting mixture of bosons and fermions in a harmonic trap. We will see that in—what is commonly called—the weakly interacting regime, interactions can still have a dramatic influence on the quantum phases. We use a mean-field approach to identify phase separation ( $a_{\text{BF}} \gg 0$ ), density enhancement ( $a_{\text{BF}} < 0$ ) and eventually the collapse of the mixture ( $a_{\text{BF}} \ll 0$ ), as a function of the Bose-Bose and Bose-Fermi interaction strength. We discuss this simple model here, first of all, because it is experimentally important to understand the density distribution of harmonically trapped Bose-Fermi mixtures prior to the lattice ramp-up. Additionally, it provides intuition to effects that are also relevant for a Bose-Fermi mixture loaded into an optical lattice. In the presence of an optical lattice the expected phases are even richer and, consequently, much less accessible by simple theoretical means.

### Self-Consistent Mean-Field Calculation

We calculate the density profiles of harmonically trapped Bose-Fermi mixtures at  $T = 0$  using a self-consistent mean-field theory [12–14]. Our model is based on the Thomas-Fermi approximation both for the bosonic and the fermionic component given in Eqs. 2.37 and 2.29, respectively. The interactions between bosons and fermions are accounted for by adding to the external trapping potential  $V_{\text{B/F}}(\mathbf{r})$ , a mean-field potential  $g_{\text{BF}}n_{\text{F}}(\mathbf{r})$  felt by the bosons and, analogously,  $g_{\text{BF}}n_{\text{B}}(\mathbf{r})$  felt by the fermions. This results in a coupled pair of equations for the bosonic and the fermionic real-space densities

$$n_{\text{B}}(\mathbf{r}) = \max \left[ \frac{\mu_{\text{B}} - V_{\text{B}}(\mathbf{r}) - g_{\text{BF}}n_{\text{F}}(\mathbf{r})}{g_{\text{BB}}}, 0 \right], \quad (2.40)$$

$$n_{\text{F}}(\mathbf{r}) = \frac{(2m_{\text{F}})^{\frac{3}{2}}}{6\pi^2\hbar^3} \Re \left[ (\mu_{\text{F}} - V_{\text{F}}(\mathbf{r}) - g_{\text{BF}}n_{\text{B}}(\mathbf{r}))^{\frac{3}{2}} \right]. \quad (2.41)$$

The Bose-Bose and the Bose-Fermi interactions in the system are parametrized by the respective scattering lengths:

$$\begin{aligned} g_{\text{BB}} &= 2\pi\hbar^2 a_{\text{BB}}/\mu_{\text{BB}}, \\ g_{\text{BF}} &= 2\pi\hbar^2 a_{\text{BF}}/\mu_{\text{BF}}, \end{aligned}$$

where  $\mu_{\text{BB}} = m_{\text{B}}/2$  and  $\mu_{\text{BF}} = (m_{\text{B}}m_{\text{F}})/(m_{\text{B}} + m_{\text{F}})$  denote the reduced masses of a colliding atom pair. The chemical potentials are implicitly determined by the bosonic and fermionic atom numbers  $N_{\text{B}}$  and  $N_{\text{F}}$  by

$$N_{\text{B/F}} = \int d\mathbf{r} n_{\text{B/F}}(\mathbf{r}, \mu_{\text{B/F}}). \quad (2.42)$$

The coupled equations are solved numerically by iteratively inserting the density distributions into the respective other equation. Conveniently, the three-dimensional problem can be reduced to one dimension in the case of a harmonic trapping potential that is equally deep (in absolute units) for the bosons and the fermions. Indeed,  $V_B(\mathbf{r}) = V_F(\mathbf{r})$  is typically a good approximation for magnetically trapped alkali atoms in the stretched hyperfine state or atoms in a far-detuned optical dipole trap (see Sect. 2.2). Introducing rescaled units

$$\tilde{x}_\alpha = \sqrt{\frac{m_B \omega_{B\alpha}^2}{2}} x_\alpha = \sqrt{\frac{m_F \omega_{F\alpha}^2}{2}} x_\alpha, \quad (2.43)$$

where  $\alpha = x, y, z$ , the external trapping potential takes the convenient form  $V_B(\tilde{\mathbf{r}}) = V_F(\tilde{\mathbf{r}}) = \tilde{\mathbf{r}}^2 = \tilde{r}^2$ . In the new coordinates the problem is spherically symmetric and therefore the density distributions solely depend on  $\tilde{r}$  instead of a three-dimensional vector  $\mathbf{r}$ . The simplified coupled equations read

$$n_B(\tilde{r}) = \max \left[ \frac{\mu_B - \tilde{r}^2 - g_{BF} n_F(\tilde{r})}{g_{BB}}, 0 \right], \quad (2.44)$$

$$n_F(\tilde{r}) = \frac{(2m_F)^{\frac{3}{2}}}{6\pi^2 \hbar^3} \Re \left[ (\mu_F - \tilde{r}^2 - g_{BF} n_B(\tilde{r}))^{\frac{3}{2}} \right] \quad (2.45)$$

and Eq. 2.42 takes the form

$$N_{B/F} = 4\pi \left( \frac{2}{m_F \bar{\omega}_F^2} \right)^{\frac{3}{2}} \int_0^\infty d\tilde{r} \tilde{r}^2 n_{B/F}(\tilde{r}, \mu_{B/F}). \quad (2.46)$$

After rescaling, the density distributions merely depend on the geometrical mean of the trapping frequencies  $\bar{\omega}_F = (\omega_{Fx} \omega_{Fy} \omega_{Fz})^{1/3}$  and the aspect ratio of the trap does not enter. Note that the results that are obtained from this set of equations are only valid within the requirements of the Thomas-Fermi approximations (see the preceding sections).

We solve the coupled equations by means of numerical iteration to obtain the density distributions  $n_B(\tilde{r})$  and  $n_F(\tilde{r})$ . The following steps are performed in this procedure:

- **Initialization:** The starting point ( $i = 0$ ) is the Thomas-Fermi profile of the pure Bose-Einstein condensate  $n_{B,0}(\tilde{r})$ . It is calculated using Eq. 2.44 with vanishing interspecies interactions ( $g_{BF} = 0$ ) and the chemical potential  $\mu_{B,0}$  being implicitly given by Eq. 2.46.
- **Start of the iteration loop:**  $n_{B,i}(\tilde{r})$  is inserted into Eq. 2.45. The resulting fermionic density profile is used to calculate the corresponding chemical potential  $\mu_{F,i+1}$  for  $N_F$  fermions using Eq. 2.46. This yields the correctly normalized fermionic density  $n_{F,i+1}(\tilde{r})$ .

- **End of iteration loop:** This new fermionic density  $n_{F,i+1}(\vec{r})$  leads to a new bosonic density distribution  $n_{B,i+1}(\vec{r})$  as a result of the interspecies interactions. It is obtained by inserting  $n_{F,i+1}(\vec{r})$  into Eq. 2.44 and matching of the bosonic chemical potential  $\mu_{B,i+1}$  to the number of bosons  $N_B$  using Eq. 2.46.

The last two steps are iteratively repeated several times (typically  $i = 1$  up to 4). The iteration can yield different outcomes: Either the procedure converges and the resulting density distributions constitute the self-consistent solutions of the problem, or the procedure diverges corresponding to an increasing central density for each iteration. The latter case can happen for attractive interspecies interactions and corresponds to a collapse of the mixture [15]. Figure 2.3 shows a summary of results obtained both for attractively and repulsively interacting Bose-Fermi mixtures at typical experimental parameters.

### 2.1.6 Routes Towards the Strongly Interacting Regime

The ratio between the interaction energy and the kinetic energy per particle determines, whether a degenerate quantum system is in the weakly or strongly interacting regime. At quantum degeneracy the de Broglie wavelength approximately corresponds to the interparticle spacing. Therefore, the de Broglie wavelength relates to the particle density via  $\lambda_{dB} \sim n^{-1/3}$  and the density dependent kinetic energy can be approximated by  $\epsilon_{kin} = \hbar^2 n^{2/3} / (2m)$ . The density dependent interaction  $\epsilon_{int} = |g|n$  has already been introduced in the preceding sections, where the interaction strength reads  $g = 4\pi \hbar^2 a_s / m$  and  $a_s$  is the scattering length (see Sect. 2.3). Accordingly, the ratio between interaction and kinetic energy per particle is given by the parameter [6]

$$\gamma = \frac{\epsilon_{int}}{\epsilon_{kin}} = \frac{|g|n}{\hbar^2 n^{2/3} / (2m)} \approx n^{1/3} |a_s|. \quad (2.47)$$

We note, that  $\gamma$  corresponds to the parameter  $k_F |a_s|$  used to characterize fermionic quantum systems, because the Fermi momentum  $k_F$  coincides with  $n^{1/3}$  in the quantum degenerate regime [4, 5].

When  $\gamma < 1$ , the quantum system is regarded as weakly interacting. In this regime interparticle correlations need not be taken into account. For example, weakly interacting bosonic quantum gases are remarkably well described within the effective single-particle theory of the Gross-Pitaevskii equation 2.35. This relatively simple framework has been successfully employed to describe exciting phenomena, such as interfering condensates or vortices [3, 6].

However, strongly correlated many-body quantum phases only arise, when  $\gamma$  exceeds unity. Equation 2.47 shows the possibilities to reach this regime: Either one increases the mass  $m$  or the interaction strength  $g$ . While these options may rather be called “impossibilities” in solid state physics, the remarkable techniques and control of atomic physics renders them possible for ultracold quantum gases.

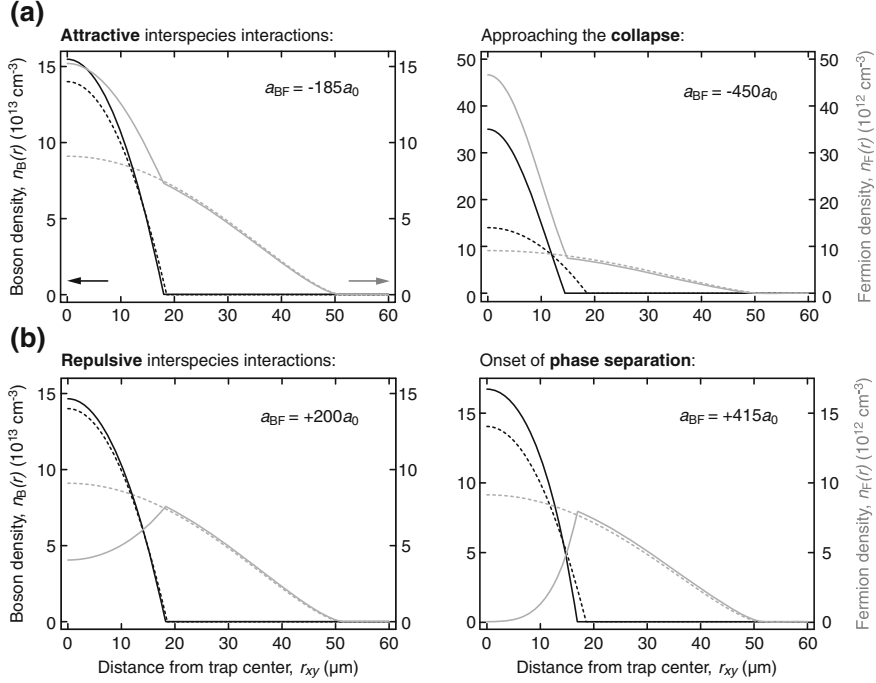


**Fig. 2.3** Real space density profiles of an interacting mixture of  $^{87}\text{Rb}$  and  $^{40}\text{K}$  in a three-dimensional harmonic trap at four interactions. The mean-field calculation has been performed assuming  $N_B = 3 \times 10^5$  bosons and  $N_F = 3 \times 10^5$  fermions and trap frequencies of  $\omega_{F_x} = \omega_{F_y} = 2\pi \times 40\text{Hz}$  in the horizontal and  $\omega_{F_z} = 2\pi \times 200\text{Hz}$  in the vertical direction, similar to the experimental situation of Chap. 8. Black (gray) lines indicate bosonic (fermionic) profiles and  $r_{xy} = \sqrt{x^2 + y^2}$ . Note the factor of ten between the units of  $n_B$  and  $n_F$ . Dashed lines show the profiles at vanishing interactions. Strikingly, the fermionic cloud is much larger than the bosonic cloud with the same atom number; the volume of the clouds differs by a factor of about twenty! This is a remarkable manifestation of the different quantum statistics. **a** At attractive interspecies interactions the atomic density accumulates in the center until the system undergoes a mean-field collapse, when the interspecies attraction is increased beyond  $a_{BF} \approx -450 a_0$ . Note that  $a_{BF} = -185 a_0$  approximately corresponds to the background scattering length between  $^{87}\text{Rb}$  and  $^{40}\text{K}$  (see Sect. 2.3.5). **b** In the case of repulsive interactions the fermions are pushed out from the trap center. The bosonic cloud is compressed by the surrounding fermions and shows an increased density in the trap center. When the interspecies repulsion is raised beyond  $a_{BF} = +415 a_0$  the central fermionic density vanishes. At this point the central bosonic density is enhanced by about 20 %

We discuss in the next two sections, how, on the one hand, an optical lattice potential can be employed to change the effective mass of atoms, and how, on the other hand, Feshbach resonances can serve as a direct control knob of the interaction strength  $g$  via the scattering length  $a_s$ .

Those two approaches have led to wonderful studies in ultracold atom physics within the last ten years. Seminal results have been the realization of the superfluid



to Mott insulator transition in an optical lattice [16, 17] or the investigation of the BEC-BCS crossover in quantum degenerate fermionic spin mixtures [18–21]. The experiments in this thesis utilize both techniques simultaneously.

## 2.2 Optical Lattice Potentials

This section briefly reviews the theory of optical lattice potentials [7]. After an introduction to optical dipole forces [22], we explain how optical standing waves can be employed to create simple cubic lattice potentials for ultracold atoms. We analyze, compare and model the landscape of realistic lattice potentials, in particular focussing on the differences of using red- or blue-detuned laser light to create the underlying optical standing waves. The section concludes with a discussion of the band structure in simple cubic lattices [23].

### 2.2.1 Optical Dipole Potentials

A light field can act on neutral atoms both in a dissipative and a conservative way. A dissipative force arises from the absorption and subsequent reemission of photons. This process can transfer net momentum on the atoms and creates a force that is often called radiation pressure. It is used for laser cooling and magneto-optical traps, where temperatures down to 100  $\mu\text{K}$  can be achieved with Doppler cooling techniques. Sub-Doppler techniques even allow to reach the microkelvin regime, at least theoretically [22, 24].<sup>5</sup> A conservative force, the so-called optical dipole force, originates from the interaction of a light field with the electric dipole moment that is induced in the atom by the very same light field. This interaction results in a shift of the atomic energy levels, the AC-Stark shift, that is proportional to the intensity of the field.

When neutral atoms are exposed to light generally both of the aforementioned forces are present. However, we will show in this section that the conservative part can play the dominating role, when the light field is far detuned from all atomic resonances. The large detuning suppresses scattering of photons more strongly than the interaction with the self-induced dipole. As the optical dipole potential is proportional to the intensity of the light field, an appropriately engineered intensity distribution allows for the creation of optical dipole traps [25] or optical lattice potentials [7, 23]. Typical depths of optical dipole potentials reach several microkelvin. Therefore, they are well suited to capture atoms that have been cooled by radiation pressure in a first step.

---

<sup>5</sup> The Doppler temperature is given by the energy scale defined by the natural linewidth  $\Gamma$  of the transition that is used for cooling,  $T_D = \hbar\Gamma/(2k_B)$ . The minimal temperature that can principally be reached with sub-Doppler techniques is set by the recoil energy, corresponding to the recoil temperature  $T_{SD} = (\hbar k)^2/(2mk_B)$ .

## Oscillator Model

We assume an atom to be exposed to a monochromatic light field  $\mathbf{E}$  that oscillates at a frequency  $\omega$ . This induces an electric dipole moment proportional to the electric field  $\mathbf{d}(\omega) = \alpha(\omega)\mathbf{E}$ . The proportionality constant  $\alpha(\omega)$  is called the polarizability. It is a function of the frequency  $\omega$  and generally takes a complex value, i.e. it also contains information on a phase shift between the electric field and the induced dipole. The potential energy of the self-induced dipole is given by

$$V_{\text{dip}} \propto -\langle \mathbf{d} \cdot \mathbf{E} \rangle \propto -\Re[\alpha(\omega)] \cdot I, \quad (2.48)$$

where  $\langle \dots \rangle$  denotes the temporal average over the fast oscillation of the light field. This is the conservative dipole potential that is proportional to the intensity  $I = \epsilon_0 c E^2 / 2$ , where the amplitude of the electric field is given by  $E = |\mathbf{E}|$  and  $c$  is the speed of light. The real part of the polarizability indicates that the in-phase component of the oscillating dipole moment is responsible for the dipole force. Conversely, the imaginary part of the polarizability denotes the out-of-phase component that gives rise to the spontaneous scattering rate

$$\Gamma_{\text{sc}} \propto \Im[\alpha(\omega)] \cdot I. \quad (2.49)$$

An expression for the polarizability can be derived using classical [26], semi-classical or fully quantized theories [27–29]. However, it turns out that for a two-level system in the limit of low saturation, also the quantum mechanical approaches yield the polarizability

$$\alpha(\omega) = 6\pi\epsilon_0 c^3 \frac{\Gamma/\omega_0^2}{\omega_0^2 - \omega^2 - i(\omega^3/\omega_0^2)\Gamma}, \quad (2.50)$$

which is conveniently derived for a classical damped oscillator [25]. Here,  $\omega_0$  denotes the optical transition frequency of the atom and  $\Gamma$  the damping rate associated with the spontaneous decay rate of the excited level (corresponding to the line width of the transition). The limit of low saturation, i.e. negligible population in the excited level, is reached at far detuning<sup>6</sup>  $\Delta = \omega - \omega_0$ , which is typically the case for dipole traps, and also implies that  $\Gamma_{\text{sc}} \ll \Gamma$  as we will see below. While the classical derivation yields an accurate description for  $\alpha(\omega)$ , this is not the case for the damping rate  $\Gamma$ . In a semi-classical derivation it turns out that the damping rate is determined by the dipole matrix element between the ground and excited state  $\Gamma \propto |\langle e|\mathbf{d}|g\rangle|^2$ .

Based on the above expressions, it is possible to derive the dipole potential and the scattering rate in the limit of large detuning and negligible saturation:

$$V_{\text{dip}}(\mathbf{r}) = -\frac{3\pi c^2}{2\omega^3} \left( \frac{\Gamma}{\omega_0 - \omega} + \frac{\Gamma}{\omega_0 + \omega} \right) \cdot I(\mathbf{r}), \quad (2.51)$$

---

<sup>6</sup> In the picture of the Bloch sphere this corresponds to a Bloch vector that only oscillates close to the ground state.

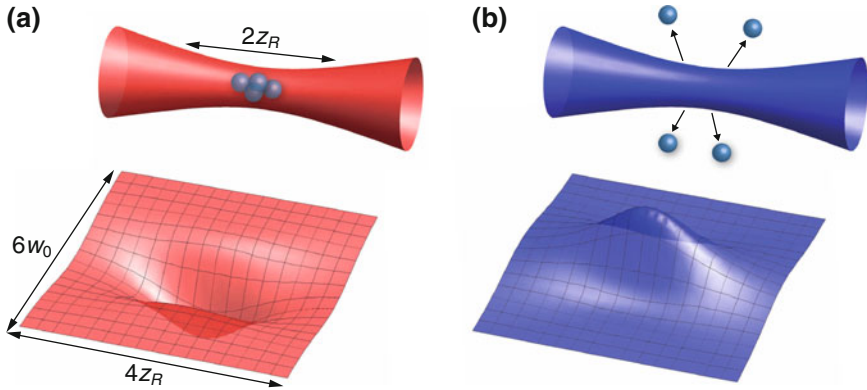


**Fig. 2.4** The *lower* pictures schematically show the dipole potential in the focus of a round *red*-**(a)** and *blue*-detuned **(b)** Gaussian laser beam. The envelope area of the *upper* images is defined by the beam radius  $w(z)$ . A *red*-detuned beam can act as a trap for ultracold atoms, while the *blue* beam creates a repulsive potential

$$\Gamma_{\text{sc}}(\mathbf{r}) = \frac{3\pi c^2}{2\hbar\omega_0^3} \left( \frac{\omega}{\omega_0} \right)^3 \left( \frac{\Gamma}{\omega_0 - \omega} + \frac{\Gamma}{\omega_0 + \omega} \right)^2 \cdot I(\mathbf{r}). \quad (2.52)$$

For the case of large, but not too large detuning  $|\Delta| \ll \omega_0$ , one may neglect the terms proportional to  $1/(\omega_0 + \omega)$  corresponding to the often employed rotating wave approximation [26, 28]. This yields the simplified formulas

$$V_{\text{dip}}(\mathbf{r}) = \frac{3\pi c^2}{2\omega_0^3} \frac{\Gamma}{\Delta} \cdot I(\mathbf{r}), \quad (2.53)$$

$$\Gamma_{\text{sc}}(\mathbf{r}) = \frac{3\pi c^2}{2\hbar\omega_0^3} \left( \frac{\Gamma}{\Delta} \right)^2 \cdot I(\mathbf{r}). \quad (2.54)$$

Those two expressions contain the physics of optical dipole potentials in a concise form. We see that  $V_{\text{dip}}$  is proportional to  $I/\Delta$ , while the scattering rate  $\Gamma_{\text{sc}}$  scales as  $I/\Delta^2$ . The sign of the detuning determines, whether the dipole potential is repulsive ( $\Delta > 0$ , blue detuning) or attractive ( $\Delta < 0$ , red detuning). Furthermore, we note that  $\Gamma_{\text{sc}}$  is proportional to  $V_{\text{dip}}/\Delta$ . This shows that inelastic scattering can be efficiently suppressed by choosing a large detuning  $\Delta$ . When optical dipole forces are employed for ultracold atoms, it is crucial to minimize inelastic scattering; the recoil energy of a single scattering process corresponds to a temperature of several 100 nK and creates strong heating compared to the motional ground state energy of the atoms. Therefore, the detuning should generally be chosen as large as possible within the limits of available laser power to ensure a conservative potential.

Although being conceptually appealing, the approximate Eqs. 2.53 and 2.54 must be taken with a grain of salt, when it comes to actual calculations. Considering the

case of rubidium, the error originating from the rotating wave approximation for the dipole potential depth amounts to 3 % for  $\lambda = 738 \text{ nm}$  (used for the optical lattice in this thesis) and even 12 % for  $\lambda = 1030 \text{ nm}$  (used for the dipole trap in this thesis). Therefore, in most cases the rotating wave approximation must not be applied. Furthermore, for  $^{40}\text{K}$  and  $^{87}\text{Rb}$ , which are used in the experiment, the fine structure splitting due to the spin-orbit coupling must be taken into account [25] leading to the  $D_1$  and  $D_2$  line doublet, which is present in all alkali atoms. For linearly polarized light, the resulting formula for the dipole potential reads

$$V_{\text{dip}}(\mathbf{r}) = \frac{\pi c^2}{2} \left[ \frac{2\Gamma_{D_2}}{\omega_{D_2}^3} \left( \frac{1}{\Delta_{D_2}} - \frac{1}{\Delta_{D_2} + 2\omega_{D_2}} \right) + \frac{\Gamma_{D_1}}{\omega_{D_1}^3} \left( \frac{1}{\Delta_{D_1}} - \frac{1}{\Delta_{D_1} + 2\omega_{D_1}} \right) \right] \cdot I(\mathbf{r}), \quad (2.55)$$

where  $\Gamma_x$  denotes the line width and  $\Delta_x = \omega - \omega_x$  the detuning of the laser frequency  $\omega$  from the respective resonance frequency  $\omega_x$  of the  $x = D_1, D_2$  line. The corresponding data for  $^{40}\text{K}$  and  $^{87}\text{Rb}$  are provided in the Appendices A.1 and A.2. For circularly polarized light, the dipole potential is also sensitive to the hyperfine splitting and depends on the quantum numbers  $F$  and  $m_F$  of Zeeman sublevels in the ground state [25]. However, using linear polarization the optical dipole force offers an elegant way to create identical potentials for different Zeeman sublevels without differential shifts. This is particularly relevant for the experiments using spin mixtures of  $^{40}\text{K}$  reported in Chap. 6.

### Red-Detuned Dipole Trap

It is conceptually simple to create a trap for ultracold atoms based on the optical dipole force discussed above. For red detuning the force is attractive and atoms are drawn towards the intensity maximum. Therefore, the focus of a single red-detuned Gaussian laser beam can be used to create a three-dimensional trapping potential for atoms (see Fig. 2.4). The intensity distribution of an elliptical Gaussian beam propagating along the  $z$ -axis, can be written as [30]

$$I(\mathbf{r}) = \frac{2P}{\pi w_x(z)w_y(z)} e^{-\frac{2x^2}{w_x^2(z)} - \frac{2y^2}{w_y^2(z)}}, \quad (2.56)$$

where  $P$  is the total power of the beam, giving rise to a peak intensity  $I_0 = 2P/(\pi w_{0x}w_{0y})$ . The beam radius  $w_\alpha(z)$  ( $\alpha = x, y$ ) denotes the distance from the beam center at which the intensity has dropped by a factor  $1/e^2$ . It is given by

$$w_\alpha(z) = w_{0\alpha} \sqrt{1 + \left( \frac{z}{z_{R\alpha}} \right)^2}, \quad (2.57)$$

where  $w_{0\alpha}$  is the beam waist along the directions  $\alpha = x, y$  and  $z_{R\alpha} = \pi w_{0\alpha}^2 / \lambda$  defines the Rayleigh length;  $\lambda$  is the wavelength of the laser light. The trapping potential that is created by a Gaussian beam profile can be approximated in the vicinity of the focus by

$$V_{\text{dip}}(\mathbf{r}) \approx -V_0 \left[ 1 - 2 \left( \frac{x}{w_{0x}} \right)^2 - 2 \left( \frac{y}{w_{0y}} \right)^2 - \frac{1}{2} \left( \frac{z}{z_{Rx}} \right)^2 - \frac{1}{2} \left( \frac{z}{z_{Ry}} \right)^2 \right]. \quad (2.58)$$

This corresponds to a harmonic trap with radial and axial trap frequencies

$$\omega_x = \sqrt{\frac{4V_0}{m w_{0x}^2}}, \quad \omega_y = \sqrt{\frac{4V_0}{m w_{0y}^2}} \quad \text{and} \quad \omega_z = \sqrt{\frac{V_0}{m} \left( \frac{1}{z_{Rx}^2} + \frac{1}{z_{Ry}^2} \right)}, \quad (2.59)$$

where  $m$  denotes the atomic mass. For typical parameters the radial trap frequencies  $\omega_x$  and  $\omega_y$  are about two orders of magnitude larger than the axial trap frequency  $\omega_z$ . Therefore a Gaussian single beam trap is highly anisotropic and hard to handle experimentally without additional axial confinement.

## 2.2.2 Optical Lattice Potentials

Optical lattice potentials for ultracold atoms are created by interfering counterpropagating Gaussian laser beams. Using one, two or three of such standing waves 1D, 2D and 3D optical lattices can be formed. For blue or red detuning the atoms are either trapped in the intensity minima or maxima, respectively, which has a subtle influence on the details of the global potential landscape.

### 1D Optical Lattice Potential

When a Gaussian beam with a wavelength  $\lambda$  is retroreflected into itself, an optical standing wave with a periodicity of  $\lambda/2$  forms (see Fig. 2.5). Such a standing wave can be used as a one-dimensional (1D) optical lattice potential for atoms. Typically, the axial extend of the atom cloud is much smaller than the Rayleigh length  $z_R$ , such that the axially dependent beam radius can be approximated by the constant beam waist  $w_z$ .<sup>7</sup> The resulting periodic potential is given by

$$V_{1D}(\mathbf{r}) = V_z e^{-2\frac{r_{xy}^2}{w_z^2}} \cos^2(kz) \simeq V_z \left( 1 - 2\frac{r_{xy}^2}{w_z^2} \right) \cos^2(kz), \quad (2.60)$$

---

<sup>7</sup> From now on we use the convention that the index of the beam waist denotes the propagation direction of the rotationally symmetric lattice beam, i.e.  $w_z$  is the waist of a round beam propagating in  $z$ -direction.



**Fig. 2.5** An optical standing wave formed by retroreflection of a Gaussian laser beam creates a one-dimensional optical lattice potential. Generally, the electric field amplitude of the returning beam is reduced by a factor, which we call the effective reflection coefficient  $\rho$

where  $k = 2\pi/\lambda$  is the wavevector of the laser light,  $r_{xy} = \sqrt{x^2 + y^2}$  is the radial coordinate and  $V_z$  is the depth of the optical lattice potential. We note that the depth of the lattice  $V_z$  is four times larger compared to the potential depth of the bare Gaussian beam without retroreflection. This enhancement is caused by constructive interference, which becomes obvious, when the counterpropagating beams are viewed on the level of electric fields. Usually, the depth of an optical lattice is given in units of the recoil energy  $E_{\text{rec}} = \hbar^2 k^2 / (2m)$ . In the following, we also use the dimensionless lattice depth  $s_z = V_z / E_{\text{rec}}$ .

In the above description of a 1D optical lattice, we have made the implicit assumption that the retroreflected beam has the same electric field amplitude as the incoming part. In experimental realizations, however, the returning part has passed through several additional optical elements reducing the field amplitude. We account for this by introducing an effective reflection coefficient  $\rho_z$  that quantifies the ratio of the returning and the incoming electric field amplitudes at the position of the atoms. For  $0 \leq \rho_z < 1$  the standing wave is not fully modulated anymore and reads

$$V_{\text{ID}}(\mathbf{r}) = \frac{V_z}{4} e^{-2\frac{r_{xy}^2}{w_z^2}} \left( 1 + \rho_z^2 + 2\rho_z \cos(2kz) \right) \quad (2.61)$$

$$\simeq \frac{V_z}{4} \left( 1 - 2\frac{r_{xy}^2}{w_z^2} \right) \left( 1 + \rho_z^2 + 2\rho_z \cos(2kz) \right). \quad (2.62)$$

For perfect reflectivity ( $\rho_z = 1$ ) Eq. 2.60 is recovered using  $\cos(2kz) = 2\cos^2(kz) - 1$ .

### External Potential of a 1D Optical Lattice

The Gaussian beam shape and finite modulation of the standing wave give rise to a transverse underlying potential in addition to the axial modulation of the optical lattice. We aim at an effective description of the lattice potential according to

$$V_{\text{ID}}(\mathbf{r}) = V'_z \cos^2(kz) + \frac{1}{2} m \omega_{xy}^2 r_{xy}^2. \quad (2.63)$$

Here,  $V'_z = \rho_z V_z$  is the effective lattice depth and  $\omega_{xy} = \omega_x = \omega_y$  the transverse trap frequency of a spherically symmetric beam. We distinguish two contributions to the frequency  $\omega_{xy}$ :

First, we use Eq. 2.62 to derive the transverse curvature of the lattice potential as it is felt by the atoms. It is crucial to distinguish red ( $V_z < 0$ ) and blue detuning ( $V_z > 0$ ) of the laser light, because in the first case the atoms are trapped in the intensity maxima for which  $\cos(2kz) = 1$ , while in the second case the atoms sit in the intensity minima described by  $\cos(2kz) = -1$ . From this, we obtain the first contribution to the transverse potential

$$\omega_{\text{pot},xy}^2 = -\frac{V_z}{m} \frac{(1 + \rho_z^2 \pm 2\rho_z)}{w_z^2}, \quad (2.64)$$

where the upper (lower) sign denotes red (blue) detuning. For a positive (negative) overall sign the potential is (anti)confining (see Fig. 2.6).

The second contribution is more subtle. Viewing a single lattice well as an harmonic oscillator potential in the axial direction, that is approximating  $\cos(2kz)$  harmonically, we obtain for the trap frequency in a lattice well at the center of the beam ( $r_{xy} = 0$ )

$$\omega_{\text{lat},z}^2 = \frac{2k^2}{m} |V'_z|. \quad (2.65)$$

Due to the Gaussian beam shape the absolute modulation depth of the standing wave radially goes down according to the factor  $\exp(-2r_{xy}^2/w_z^2)$ . Consequently, the trap frequency on a lattice well decreases like

$$\omega_{\text{lat},z}(r_{xy}) = \omega_{\text{lat},z} e^{-\frac{r_{xy}^2}{w_z^2}} \approx \omega_{\text{lat},z} \left(1 - \frac{r_{xy}^2}{w_z^2}\right) \quad (2.66)$$

in the transverse direction and so does the ground state energy  $E_0(r_{xy}) = \hbar\omega_{\text{lat},z}(r_{xy})/2$  of the local harmonic oscillator. This gives rise to an additional radial anticonfinement that is independent of the sign of the laser detuning. Hence, the frequency originating from the shift in the harmonic ground state energy reads

$$\omega_{\text{ho},xy}^2 = -\frac{2}{mw_z^2} \sqrt{|V'_z| E_{\text{rec}}}. \quad (2.67)$$

Combining the two contributions and introducing the dimensionless effective lattice depth  $s'_z = V'_z/E_{\text{rec}}$ , the transverse trap frequency of the external potential reads

$$\omega_{xy}^2 = -\frac{E_{\text{rec}}}{mw_z^2} \left[ \left( \frac{1}{\rho_z} + \rho_z \pm 2 \right) s'_z - 2\sqrt{s'_z} \right], \quad (2.68)$$

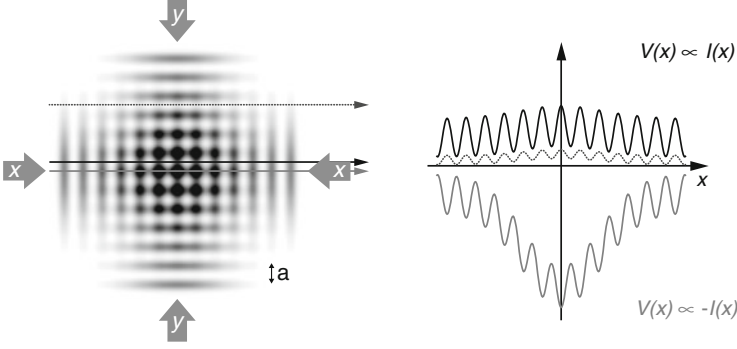


**Fig. 2.6** External trapping potential for *red*- and *blue*-detuned lattices. The intensity distribution of a 3D lattice with reduced reflectivity ( $\rho = 0.25$ ) of the retro beam is shown as a density plot. Cuts show the influence of the perpendicular beams on the lattice potential along the  $x$  axis. In the case of *blue* detuning the cut is taken for  $I(x, a/2, a/2)$  (black) and  $I(x, 7a/2, a/2)$  (dotted), while for *red* detuning the cut corresponds to  $I(x, 0, 0)$  (gray). The underlying confinement of the *red* lattice is much stronger than the corresponding anticonfinement of the *blue* lattice

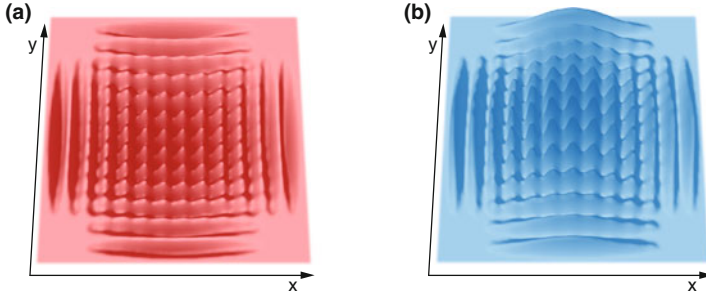


**Fig. 2.7** Comparison of the lattice potentials created by a *red*- (a) and *blue*-detuned (b) laser. In a *red* lattice the potential minima are located at the intensity maxima as  $V(\mathbf{r}) \propto -I(\mathbf{r})$ , while in a *blue* lattice the potential minima are located at the intensity minima as  $V(\mathbf{r}) \propto I(\mathbf{r})$

where the upper (lower) sign holds for red (blue) detuning. In typical experimental setups the effective reflection coefficient does not exceed the range  $0.8 < \rho_z < 1$ . For those values the prefactor  $1/\rho_z + \rho_z \pm 2$  is very close to 4 (zero) for the case of red (blue) detuning. Therefore, a red-detuned lattice has an underlying external potential that consists of a dominant confining term (scaling as  $s_z'$ ) and an anticonfining term (scaling as  $\sqrt{s_z'}$ ). In a blue-detuned lattice, however, both terms are anticonfining and the  $\sqrt{s_z'}$  scaling dominates. This important result is confirmed by direct measurements of the transverse external potential in a blue-detuned optical lattice presented in Sect. 5.4 (Fig. 2.7).



### 3D Optical Lattice Potential

A simple cubic optical lattice potential can be created by crossing three optical standing waves orthogonally to each other. In order to suppress interference between the three standing waves it is crucial to choose mutually orthogonal linear polarizations. However, in the experiment slight deviations of the polarizations and resulting small interferences are hard to avoid. Such interferences can be rendered harmless by choosing laser frequencies of the beams that differ by some tens of MHz. This leads to rapid oscillations of spurious potential corrugations and the atoms effectively feel a smooth lattice potential due to time averaging. Therefore, we can assume independent 1D optical lattices in  $x$ ,  $y$  and  $z$  direction, which create a 3D optical lattice potential of simple cubic type with a lattice constant of  $\lambda/2$  and a one atom basis. Using Eq. 2.61 the 3D optical lattice potential can be written as

$$\begin{aligned}
 V_{3D}(\mathbf{r}) = & \frac{V_x}{4} e^{-2\frac{r_{yz}^2}{w_x^2}} \left(1 + \rho_x^2 + 2\rho_x \cos(2kx)\right) \\
 & + \frac{V_y}{4} e^{-2\frac{r_{xz}^2}{w_y^2}} \left(1 + \rho_y^2 + 2\rho_y \cos(2ky)\right) \\
 & + \frac{V_z}{4} e^{-2\frac{r_{xy}^2}{w_z^2}} \left(1 + \rho_z^2 + 2\rho_z \cos(2kz)\right).
 \end{aligned} \tag{2.69}$$

Here,  $V_\alpha$  denote the potential depth,  $w_\alpha$  the waist and  $\rho_\alpha$  the effective reflectivity of the superimposed 1D standing waves ( $\alpha = x, y, z$ ). As above, red (blue) detuning corresponds to  $V_\alpha < 0$  ( $V_\alpha > 0$ ).

### External Potential of 3D Optical Lattices

It is convenient to approximate the 3D optical lattice potential in the center, for distances much smaller than the beam waists, as a sum of a homogeneous periodic modulation and an external harmonic potential according to

$$V_{3D}(\mathbf{r}) \simeq V'_x \cos^2(kx) + V'_y \cos^2(ky) + V'_z \cos^2(kz) + \frac{1}{2}m(\omega_x^2 x^2 + \omega_y^2 y^2 + \omega_z^2 z^2). \tag{2.70}$$

Here, the effective lattice depths are denoted by  $V'_\alpha = \rho_\alpha V_\alpha$  and  $\omega_\alpha$  are the effective trap frequencies of the external harmonic potential in the directions  $\alpha = x, y, z$ . Using the above results for the 1D case, the squared trap frequencies are readily derived and read

$$\omega_x^2 = -\frac{E_{\text{rec}}}{m} \left[ \frac{(1/\rho_y + \rho_y \pm 2) s'_y - 2\sqrt{s'_y}}{w_y^2} + \frac{(1/\rho_z + \rho_z \pm 2) s'_z - 2\sqrt{s'_z}}{w_z^2} \right]. \tag{2.71}$$

The corresponding expressions for  $\omega_y^2$  and  $\omega_z^2$  are obtained by cyclic permutation of the indices. Assuming an isotropic potential, for which the dimensionless effective lattice depths  $s'_\alpha = s'$ , the effective reflectivities  $\rho_\alpha = \rho$ , the waists  $w_\alpha = w$  are equal in all directions  $\alpha = x, y, z$  and  $r^2 = x^2 + y^2 + z^2$ , the entire external potential can be expressed by

$$V_{3D}^{\text{ext}}(\mathbf{r}) = -E_{\text{rec}} \left[ \left( \frac{1}{\rho} + \rho \pm 2 \right) s' - 2\sqrt{s'} \right] \frac{r^2}{w^2} \quad (2.72)$$

This expression contains both the effects of finite effective reflectivity as well as the anticonfinement scaling as  $\sqrt{s'}$  that originates from the transverse change of the ground state energy for each lattice beam. In the case of a blue-detuned 3D optical lattice (lower sign), which is used in the experiments of this thesis, the later term is dominating the external potential of the lattice.

### 2.2.3 Band Structure and Bloch States

In this section we derive the eigenstates of a single particle that moves in a periodic potential. The corresponding eigenenergies form energy bands with a characteristic structure depending on the symmetries and the depth of the lattice. Irrespective whether an electron in an ionic crystal or an atom in an optical lattice is the matter of interest, the resulting physics is identical. However, we want to emphasize two caveats on the theory derived in this section:

- First, it refers to a homogeneous lattice system that extends to infinity. This is a reasonable assumption for large solid state crystals, but in the case of finite-sized optical lattices it must be handled with care. Deviations that arise in an optical lattice with an underlying confining potential are numerically addressed in Sect. 3.3.3.
- Second, what is derived in this section is a single-particle theory. Therefore, the theory itself and all implications that are drawn from it are strictly speaking only valid for single particles or noninteracting many-particle systems. Noninteracting systems can be realized with ultracold atoms using spin polarized fermions, which do not collide in the low energy limit, or by tuning the scattering length to zero using a Feshbach resonance (see Sect. 2.3). However, essentially all experiments of this thesis feature interacting particles.

Nevertheless, the single-particle band structure of homogeneous lattices is the basis to understanding the physics of more involved interacting systems. Band structure in conjunction with quantum statistics often allows to understand basic physical effects in lattices, such as the formation of metallic or band insulator states for fermions [31] (see Chap. 6).

The optical lattice used in the experiments has a three-dimensional simple cubic structure. Therefore, the movement of the atoms can be considered independently for

the three coordinate axes  $x$ ,  $y$  and  $z$ . It is sufficient to solve the Schrödinger equation of the one-dimensional problem:

$$\hat{H}\phi_q^{(n)}(x) = E_q^{(n)}\phi_q^{(n)}(x) \quad \text{with} \quad \hat{H} = \frac{\hat{p}^2}{2m} + V(x), \quad (2.73)$$

where  $\hat{p} = -i\hbar\partial/\partial x$  is the momentum operator and  $V(x)$  is assumed to be a homogeneous lattice potential with periodicity  $a = \lambda/2 = \pi/k$ , where  $\lambda$  is the wavelength of the laser creating the lattice. According to Bloch's theorem [31] each eigenstate  $\phi_q^{(n)}(x)$  of this Hamiltonian can be written as a product of a plane wave with wavevector  $q$  and a function  $u_q^{(n)}(x) = u_q^{(n)}(x + a)$  with the same periodicity as the lattice potential,

$$\phi_q^{(n)}(x) = e^{iqx/\hbar} u_q^{(n)}(x). \quad (2.74)$$

We use this wavefunction as an ansatz and insert it into Eq. 2.73 to obtain an eigenvalue problem for  $u_q^{(n)}(x)$ :

$$\hat{H}_q u_q^{(n)}(x) = \left( \frac{1}{2m} (\hat{p} + q)^2 + V(x) \right) u_q^{(n)}(x) = E_q^{(n)} u_q^{(n)}(x). \quad (2.75)$$

At this point we can use the fact that both the potential  $V(x)$  and the functions  $u_q^{(n)}(x)$  have the same periodicity. They can be expanded in discrete Fourier sums consisting of plane waves with wavevector  $2k$  and the corresponding higher harmonics:

$$V(x) = \sum_r V_r e^{i2krx} \quad \text{and} \quad u_q^{(n)}(x) = \sum_s c_s^{(n,q)} e^{i2ksx}, \quad (2.76)$$

where the indices  $r, s$  run over all integer numbers. Based on the expansion of  $u_q^{(n)}(x)$  it becomes apparent, that the Bloch function  $\phi_q^{(n)}(x)$  can be constructed by a superposition of plane waves with wavevectors  $q/\hbar + 2ks$ , where  $2ks$  are the reciprocal lattice vectors [31]. This implies, that the quasi-momenta  $q$  that give rise to distinct Bloch functions are restricted to the interval  $[-\hbar k, \hbar k]$ . This interval is called the first Brillouin zone. For each value of  $q$  we can expect an infinite number of discrete energy levels  $E_q^{(n)}$  that are conveniently labeled by the positive integer index  $n$ . It will become clear below, why  $n$  is called the band index.

Inserting the Fourier sums into Eq. 2.75, we obtain for the kinetic energy

$$\frac{1}{2m} (\hat{p} + q)^2 u_q^{(n)}(x) = \sum_s \frac{(2\hbar ks + q)^2}{2m} e^{i2ksx} c_s^{(n,q)} \quad (2.77)$$

and the potential energy

$$V(x) u_q^{(n)}(x) = \sum_r \sum_{s'} V_r e^{i2k(r+s')kx} c_{s'}^{(n,q)} = \sum_r \sum_s V_r e^{iksx} c_{s-r}^{(n,q)}. \quad (2.78)$$

The functional form of an optical lattice potential is known to be sinusoidal, such that the corresponding Fourier expansion is simply given by

$$V(x) = V_x \cos^2(kx) = \frac{V_x}{4} (e^{i2kx} + e^{-i2kx} + 2) \quad (2.79)$$

with the only non-vanishing Fourier coefficients being  $V_0 = V_x/2$  and  $V_{\pm 1} = V_x/4$ . This allows to write the eigenvalue problem of Eq. 2.75 in matrix form

$$\sum_{s'} H_{ss'} c_{s'}^{(n,q)} = E_q^{(n)} c_s^{(n,q)}, \quad (2.80)$$

where  $H_{ss'}$  is the matrix of the Hamiltonian  $\hat{H}_q$  calculated with respect to the basis of plane waves  $e^{i2ksx}$ . The entries of the matrix are given by

$$H_{ss'} = \begin{cases} (2s + \frac{q}{\hbar k})^2 E_{\text{rec}} + V_x/2 & \text{if } |s - s'| = 0, \\ V_x/4 & \text{if } |s - s'| = 1, \\ 0 & \text{else.} \end{cases} \quad (2.81)$$

Here it becomes apparent, that the recoil energy  $E_{\text{rec}} = \hbar^2 k^2 / (2m)$  is the natural unit for the lattice depth  $V_x$ .

The Hamiltonian can be numerically diagonalized for a given quasi-momentum  $q$  yielding the eigenenergies  $E_q^{(n)}$  and the eigenvectors  $\mathbf{c}^{(n,q)} = (c_s^{(n,q)})$  that define the Bloch functions via Eqs. 2.76 and 2.74. The matrix entries for large indices  $|s|$  correspond to high-energy contributions (see Eq. 2.78) and the coefficients  $c_s^{(n,q)}$  become very small in the lowest bands. Therefore, it is sufficient to include the matrix entries up to a cut-off index  $|s| \leq s_{\text{max}}$ . For typical lattice depths up to  $50 E_{\text{rec}}$  it is sufficient to keep the entries with  $|s| \leq 7$ . In principle, the numerical diagonalization within the limited Hilbert space yields results for the first  $2s_{\text{max}} + 1$  bands, but the outcome is most accurate for the lowest energy bands.

The results of band structure calculations for a one-dimensional sinusoidal lattice at several depths are displayed in Fig. 2.8. For very low lattice depth the band structure does not show band gaps and corresponds to the kinetic energy of a free particle, where the dispersion parabola is reduced to the first Brillouin zone. For increasing lattice depths band gaps open up and the band width decreases exponentially in particular for the lowest lying bands. We observe that the energies  $E_q^{(n)}$  for a fixed index  $n$  are a continuous function of  $q$  being bounded from below and above, which motivates the name band index for  $n$ . In very deep lattices, the individual lattice wells become more and more independent and the low energy physics can be well described in the harmonic approximation. In this case, the gap between the lowest bands is given by the energy spacing of the on-site harmonic oscillator  $\hbar\omega_{\text{lat},x}$ .

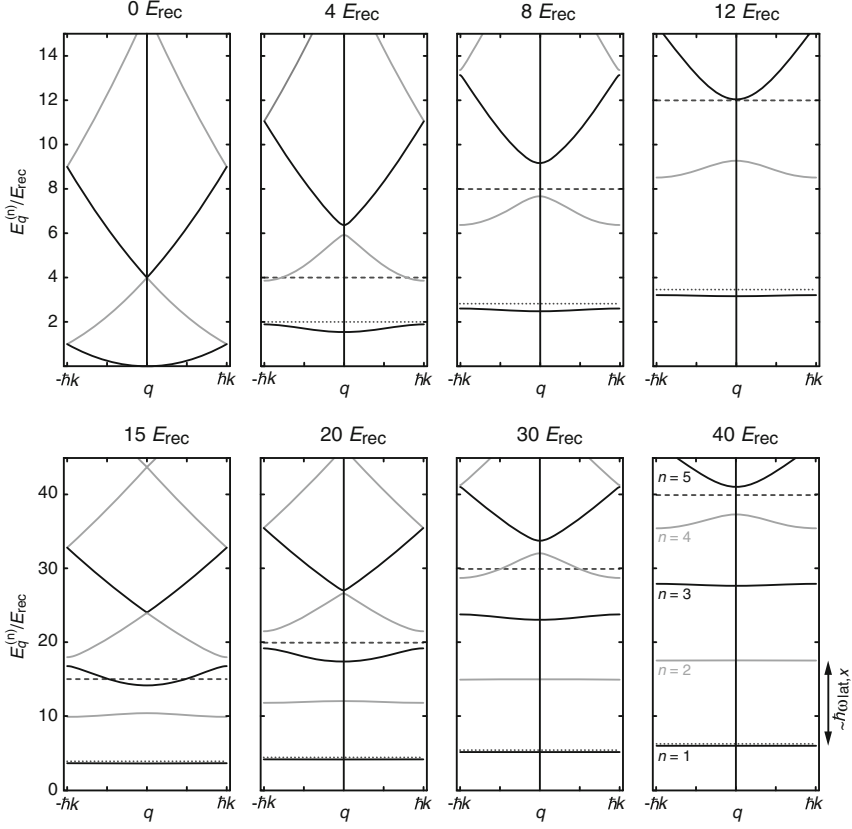


**Fig. 2.8** Band structure of a one-dimensional optical lattice. The eigenenergies  $E_q^{(n)}$  of Bloch states  $\phi_q^{(n)}$  at quasi-momenta  $q$  are displayed for the lowest bands  $n$  at several lattice depths ranging from 0 to 40  $E_{\text{rec}}$ . The lattice depths  $V_x$  are shown as *dashed lines*. *Dotted lines* indicate the zero point energy  $\hbar\omega_{\text{lat},x}/2$ , when single lattice wells are treated in harmonic approximation. For deep lattices the lowest band becomes flat and the band gap is well approximated by the level spacing of the harmonic oscillator  $\hbar\omega_{\text{lat},x}$

However, we note that even in deep lattices the higher bands with energies larger than the depth of the lattice (dashed lines in Fig. 2.8) remain wide and still closely resemble the dispersion relation of a free particle. Here, the main effect of the lattice can be captured by assigning a larger effective mass  $m_{\text{eff}} > m$  to the particle, which leads to a slower movement through the lattice potential. Generally, the effective mass at quasi-momentum  $q_0$  and band index  $n$  is given by

$$m_{\text{eff}}^{(n)}(q_0) = \hbar^2 \left( \frac{\partial^2 E_q^{(n)}}{\partial q^2} \bigg|_{q_0} \right)^{-1}. \quad (2.82)$$

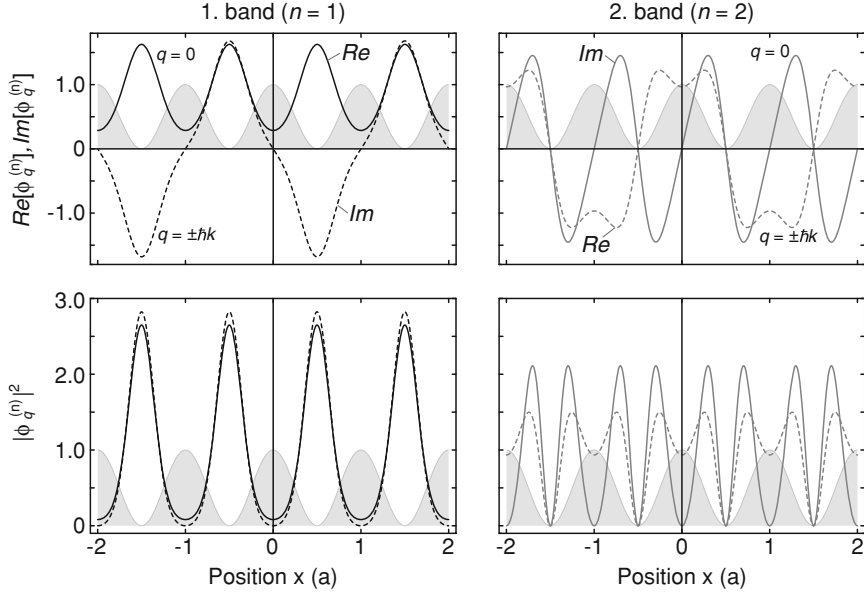


**Fig. 2.9** Exemplary Bloch wavefunctions  $\phi_q^{(n)}$  of a one-dimensional  $8 E_{\text{rec}}$  lattice. The *upper* (*lower*) panels show the probability amplitudes (probability densities) in the first and second band for the quasi-momenta  $q = 0$  (*solid lines*) and  $q = \pm \hbar k$  (*dashed lines*). The periodicity of the lattice potential is indicated by the *gray shading*

Similarly, the group velocity of a wavepacket in the Bloch state  $\phi_{q_0}^{(n)}$  is given by the first derivative of the dispersion relation [23]

$$v_{\text{gr}}^{(n)}(q_0) = \frac{1}{\hbar} \left. \frac{\partial E_q^{(n)}}{\partial q} \right|_{q_0}. \quad (2.83)$$

Examples for the Bloch wavefunctions  $\phi_q^{(n)}(x)$ , which are obtained in a band structure calculation, are shown in Fig. 2.9. Being composed of a discrete sum of plane waves, the Bloch functions are delocalized and extend over the complete, infinitely large lattice. In the lowest band ( $n = 1$ ), the Bloch state in the center of the Brillouin zone ( $q = 0$ ) is symmetric, while at the Brillouin zone edges ( $q = \pm \hbar k$ ) the wavefunction is antisymmetric. The symmetries alternate for higher bands as do the curvatures of the energy bands. The wavefunctions with the highest energy within a certain band are antisymmetric. Furthermore, Fig. 2.9 shows that the wavefunctions of the second band feature an enhanced probability of finding the particle within the potential barrier separating the lattice sites.

The Bloch states of the three-dimensional simple cubic lattice can be constructed as product wavefunctions of the one-dimensional Bloch states for each axis  $x$ ,  $y$  and  $z$ , because the Hamiltonian is fully separable. The energy of the product state is given by the sum of the eigenenergies of the three individual Bloch states. In a

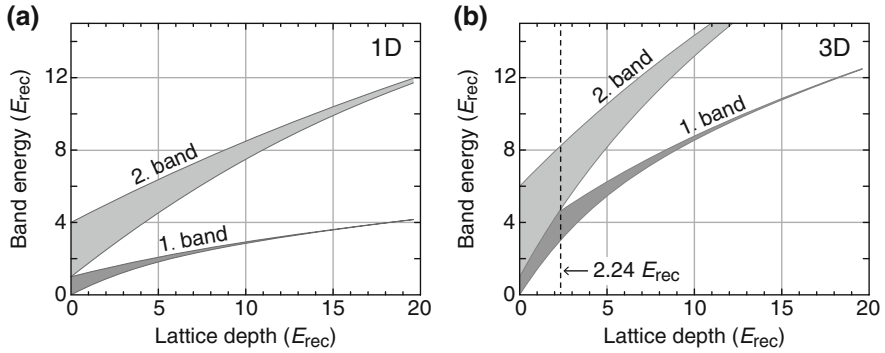


**Fig. 2.10** Bandwidths of the first and second Bloch band as a function of lattice depth in one (a) and three (b) dimensions. While the bands are fully separated in the one-dimensional case, in the three-dimensional case the band gap only starts to open at about  $2.24 E_{\text{rec}}$ . The lattice depth is assumed to be identical for each lattice axis

one-dimensional lattice the first and second Bloch band are fully separated for any nonvanishing lattice depth (see Fig. 2.10a). However, in three dimensions the first excited band corresponds to product wavefunctions of two ( $n = 1$ ) and one ( $n = 2$ ) Bloch states. For low lattice depths and certain quasi-momenta  $\mathbf{q} = (q_x, q_y, q_z)$ , those can have a lower total energy than wavefunctions of the lowest band consisting of a product of three ( $n = 1$ ) Bloch states. For a three-dimensional lattice a band gap between the lowest lattice bands starts to open for depths larger than about  $2.24 E_{\text{rec}}$  (see Fig. 2.10b).

All experiments reported in this thesis start by adiabatically loading an ultracold quantum gas or quantum gas mixture into a three-dimensional optical lattice. The lattice depths of all axes are ramped up slowly in order to ensure, that the many-body system remains in its ground state and, in particular, stays in the first lattice band. For the case of a Bose-Einstein condensate this last requirement is not very critical as the atoms dominantly accumulate in the  $q = 0$  Bloch state of the first band, which is the lowest energy state and well separated from the second band even for low lattices. However, for fermionic atoms a Fermi sea develops, in which the Bloch states of the first Brillouin zone are filled from bottom up (see Sect. 2.1). Depending on the filling of the Brillouin zone, which is determined by the system size, higher lying Bloch states may be populated, whose energy is degenerate with states of the second band. This situation bears the risk of populating the second band during lattice loading. In Chap. 6 an experimental solution to this problem is presented.

### 2.2.4 Wannier Basis

Instead of working within the basis of fully delocalized Bloch wavefunctions, it is often more convenient to use a basis set of wavefunctions that are localized at individual lattice sites. Particularly, in the limit of deep lattices the individual sites

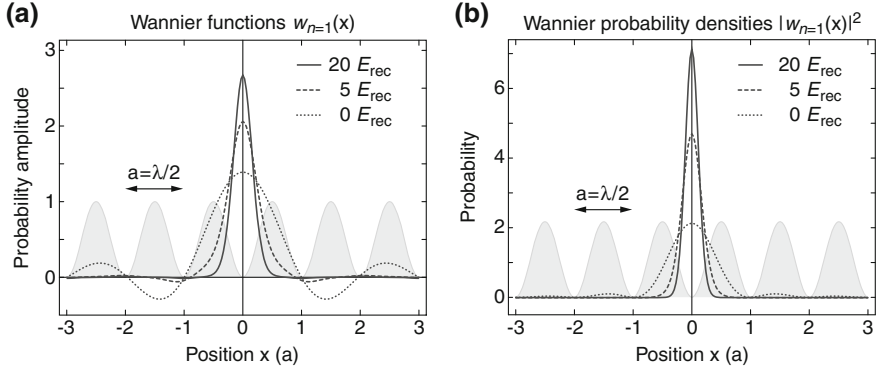


**Fig. 2.11** Wannier functions (a) and probability densities (b) at several lattice depths plotted together with the schematic lattice potential (gray shading). For deeper lattices, the Wannier functions are strongly localized. Their overlap with neighboring lattice sites is reduced, which corresponds to a suppression of tunnel coupling

are more and more decoupled from each other and the motion of atoms tends to be restricted to single wells. If the lattice is occupied by many particles, interactions may further enhance localization (see Chap. 3) (Fig. 2.11).

The Wannier functions form a basis set of maximally localized wavefunctions composed by coherent superpositions of Bloch states. The Wannier function of a localized particle at the  $j$ th lattice site in the  $n$ th Bloch band is defined by [31]

$$w_{(n)}(x - x_j) = \frac{1}{\sqrt{\mathcal{N}}} \sum_q e^{-iqx_j} \phi_q^{(n)}(x). \quad (2.84)$$

Here, the phase factor  $\exp(-iqx_j)$  compensates the factor  $\exp(iqx)$ , which appears in the definition of the Bloch states 2.74, at the coordinate  $x_j$ , inducing constructive superposition of the states  $\phi_q^{(n)}(x)$  at the corresponding lattice site. The sum runs over the quasi-momenta  $q$  within the first Brillouin zone taking discrete values, if the lattice has a finite size. Assuming normalized Bloch states in a system with  $M$  lattice sites, there are  $M$  different quasi-momenta  $q$  and the normalization is given by  $\mathcal{N} = M$ .

Because both the Bloch and Wannier wavefunctions form a basis, also the reverse transformation is possible

$$\phi_q^{(n)}(x) = \frac{1}{\sqrt{\mathcal{N}}} \sum_j e^{iqx_j} w_{(n)}(x - x_j), \quad (2.85)$$

where the summation is performed over all  $M$  lattice sites. This expression shows that the quasi-momentum  $q$  determines the phase relation between the localized wavefunctions on the individual lattice sites.



Owing to the decoupling of the spatial directions in a simple cubic lattice, the three-dimensional Wannier function for a particle in the  $n$ th band at lattice site  $\mathbf{r}_j = (x_j, y_j, z_j)$  is given by the product

$$w_{(n)}(\mathbf{r} - \mathbf{r}_j) = w_{(n)}(x - x_j) \cdot w_{(n)}(y - y_j) \cdot w_{(n)}(z - z_j) \quad (2.86)$$

of the  $n$ th band Wannier functions  $w_{(n)}(\alpha - \alpha_j)$  of the individual one-dimensional lattices ( $\alpha = x, y, z$ ). When the first Bloch band is concerned, we usually drop the band index of the Wannier function and simply write  $w(\mathbf{r} - \mathbf{r}_j)$ .

## 2.3 Feshbach Resonances

Feshbach resonances allow to control the interactions between atoms by an external magnetic field and have become one of the most important tools in ultracold atom experiments [32]. In this section we will briefly summarize the basics on interatomic interactions and Feshbach resonances as far as they are relevant to this thesis. The discussion also includes the creation of loosely bound Feshbach molecules and the effects of a tight external confinement on the collision physics of two interacting particles.

### 2.3.1 Elastic Scattering and Low Energy Collisions

As in classical mechanics, scattering of two particles in quantum mechanics is described in a coordinate system, in which the center of mass of the two particles is at rest. By doing this the problem reduces to an effective single-particle Hamiltonian in terms of the coordinate  $\mathbf{r} = \mathbf{r}_2 - \mathbf{r}_1$ , which is the relative distance between the two particles at positions  $\mathbf{r}_1$  and  $\mathbf{r}_2$ , and the reduced mass  $\mu = m_1 m_2 / (m_1 + m_2)$ . In the absence of scattering the solution would simply be a plane wave  $e^{ikz}$ , which can be chosen to propagate along the  $z$ -direction without loss of generality.  $k$  denotes the momentum of the effective particle with the reduced mass  $\mu$ . When a potential  $V(r)$ , which we assume to be spherically symmetric for simplicity ( $r = |\mathbf{r}|$ ), is introduced, there will be a finite probability for the particle to be scattered. The resulting asymptotic wavefunction at large distances has the form

$$\psi(\mathbf{r}) \propto e^{ikz} + f(\theta) \frac{e^{ikr}}{r}, \quad (2.87)$$

consisting of the incoming wave  $e^{ikz}$  and an outgoing spherical wave  $f(\theta)e^{ikr}/r$ , where the scattering amplitude  $f(\theta)$  is a function of the scattering angle  $\theta$  (and generally also of the momentum  $k$ ). Based on this wavefunction the incoming and

the outgoing probability flux can be calculated, which yields for the differential cross section

$$\frac{d\sigma}{d\Omega} = |f(\theta)|^2. \quad (2.88)$$

Since we have assumed a spherically symmetric potential, the wavefunction  $\psi(\mathbf{r})$  can be expanded in terms of spherical waves with angular momentum  $l$  and vanishing projection on the  $z$ -axis ( $m = 0$ ). In this basis the scattering amplitude takes the form [9, 33]

$$f(\theta) = \sum_{l=0}^{\infty} (2l+1) \left( \frac{e^{2i\delta_l} - 1}{2ik} \right) P_l(\cos \theta), \quad (2.89)$$

where  $P_l(\cos \theta)$  are the Legendre polynomials. The strength of this formulation lies in the fact, that the whole scattering process is captured by the parameters  $\delta_l$ , which simply denote the spatial phase shift that is added to each spherical wave with angular momentum  $l$  due to the scattering process. Using the optical theorem we can directly compute the total scattering cross section [33]

$$\sigma_{\text{tot}} = \frac{4\pi}{k} \Im[f(\theta = 0)] = \frac{4\pi}{k^2} \sum_{l=0}^{\infty} (2l+1) \sin^2 \delta_l. \quad (2.90)$$

It can be shown, that the phase shifts scale as a function of the collisional momentum  $k$  according to  $\delta_l \propto k^{2l+1}$ . This means the phase shifts for partial waves  $l \neq 0$  essentially vanish for collisions with very low momentum—and so do their contributions to the total scattering cross section. More pictorially, at low momenta, i.e. low collision energy  $E_{\text{kin}} = \hbar^2 k^2 / 2\mu$ , the effective particle is not able to penetrate the centrifugal barrier [33]. This is the second term of the effective potential  $V_{\text{eff}}(r) = V(r) + \hbar^2 l(l+1)/(2mr)$  that arises when the scattering problem is formulated in spherical coordinates. Hence, the scattering amplitude reduces to

$$f(\theta) \approx f_s = \frac{e^{2i\delta_0} - 1}{2ik} = \frac{1}{k \cot \delta_0 - ik}, \quad (2.91)$$

which is even independent of the scattering angle  $\theta$  as  $P_0(\cos \theta) = 1$ . It is possible to argue that  $k \cot \delta_0$  must be an even function of  $k$  [4, 33] and correspondingly one can introduce the expansion

$$k \cot \delta_0 \approx -\frac{1}{a_s} + \frac{1}{2} r_{\text{eff}} k^2 \quad (2.92)$$

for low momenta, where  $a_s$  denotes the  $s$ -wave scattering length and  $r_{\text{eff}}$  the effective range of the scattering potential. The effective range is typically of the order of the

van der Waals length  $r_{\text{eff}} \approx (\mu C_6/\hbar^2)^{1/4}/2$ .<sup>8</sup> For the case  $k|a_s| \ll 1$  and  $kr_{\text{eff}} < 1$  the scattering amplitude becomes independent of the momentum  $k$  reading  $f_s = -a_s$  and leads to a total cross section for  $s$ -wave collisions of

$$\sigma_{\text{tot},s} \approx 4\pi a_s^2, \quad (2.93)$$

which equals the scattering cross section of a hard sphere with a radius  $a_s$  [33].

## Identical Particles

For now we have derived the theory of collisions based on the assumption of distinguishable particles. However, indistinguishability of quantum particles and their quantum statistics have a profound impact on scattering. On the one hand, the scattering wavefunction  $\psi(\mathbf{r})$  must be spatially symmetric for two identical bosons. Therefore, only partial waves with even  $l$  enter and they enter twice due to symmetrization. The  $s$ -wave scattering cross section therefore amounts to  $\sigma_{\text{tot},s} = 8\pi a_s$ . On the other hand, the spatial wavefunction for two identical fermions must be antisymmetric as the spin wavefunction is necessarily symmetric. In this case only partial waves with odd  $l$  contribute and  $s$ -wave collisions of identical fermions are forbidden. Therefore, spin polarized ultracold Fermi gases show essentially no interactions, because scattering of higher partial waves is energetically suppressed.

## Pseudo-Potentials

Assuming that the collisional momentum is so low, that the corresponding de Broglie wavelength  $\lambda_{\text{dB}} = 2\pi/k$  is much larger than the range of the interatomic potential, the details of the potential do not matter for the scattering process. In this case it is convenient to replace the complicated full interatomic potential by a much simpler pseudo-potential that nevertheless reproduces the  $s$ -wave scattering correctly. This purpose is served by the simple contact potential operator

$$V(\mathbf{r}) = \frac{2\pi\hbar^2 a_s}{\mu} \delta(\mathbf{r}). \quad (2.94)$$

Using plane waves it is easily shown, that this expression reproduces the  $s$ -wave scattering amplitude  $f_s = -a_s$  in first Born approximation [33]. However, for practical use in three dimensions it often must be regularized to avoid  $1/r$  divergences of wavefunctions when  $r \rightarrow 0$ . This is typically done by replacing the delta function with  $\delta(\mathbf{r}) \frac{\partial}{\partial r} r$  [1, 35].

---

<sup>8</sup> References [32, 34] quote van der Waals lengths of  $64.90 a_0$  for  $^{40}\text{K}$  and  $82.58 a_0$  for  $^{87}\text{Rb}$ , where  $a_0$  denotes the Bohr radius.

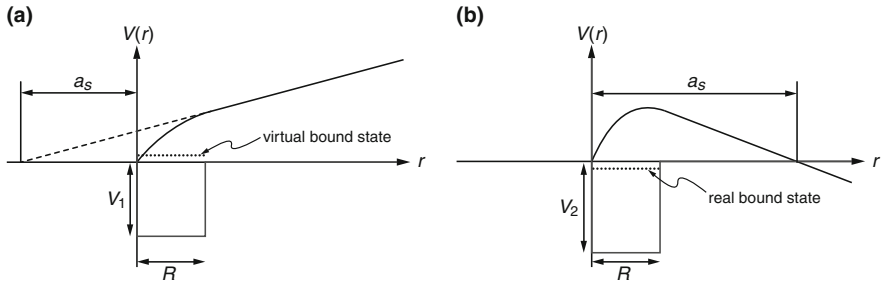


**Fig. 2.12** Scattering resonance. We assume two colliding particles with an attractive interparticle box potential  $V(r)$  with a finite range  $R$  (gray solid lines). **a** Due to the attractive potential with a depth  $V_1$  the radial wavefunction  $u(r) \propto r - a_s$  has a stronger curvature inside the range  $R$  than outside. The intercept  $a_s$  of the outside wavefunction with the abscissa corresponds to the scattering length  $a_s < 0$ . When the potential is deep enough that a bound state almost enters, the scattering length diverges  $a_s \rightarrow -\infty$ . **b** When the potential is deeper ( $V_2 < V_1$ ) and a real, very loosely bound state has just entered, the bend of the wavefunction becomes stronger and gives rise to a very large positive scattering length  $a_s$ . Thus, by tuning the position of a bound state, it can be possible to vary the scattering length over a huge range

### 2.3.2 Feshbach Resonances

The phenomenon of resonance scattering is treated in many textbooks [9, 33]. Assuming low collision momenta and modeling the attractive scattering potential by a box, it can be shown that the  $s$ -wave scattering length diverges and changes sign (from negative to positive) when the potential is deepened and a new bound state enters (see Fig. 2.12). Practically this means, that it would be possible to tune the interactions between particles when there was a knob that allowed to tune a bound state into resonance with the energy of the colliding particles.

For atoms it is not directly possible to tune the depth of the interatomic potential; however, Feshbach resonances offer an ingenious way to bring a bound state into resonance with colliding atoms simply by changing an external magnetic field (see Fig. 2.13a). Let us assume that two (distinguishable) atoms in the hyperfine states  $|F_1, m_{F_1}\rangle$  and  $|F_2, m_{F_2}\rangle$  collide with a very low relative kinetic energy in the entrance channel (also called: open channel). The atoms can perform  $s$ -wave scattering into scattering channels that conserve  $M = m_{F_1} + m_{F_2}$  [32]. However, those scattering channels typically have a different magnetic moment than the open channel as they correspond to a different spin configuration. By varying the external magnetic field, it can thus be possible to tune a bound state of one of the scattering channels (also called: closed channel) into resonance with the open channel. If there was no coupling between the open and the closed channel, the atoms would just acquire a phase shift corresponding to the open potential. They would scatter off each other without resonance effects. However, the spin configurations of the open and the closed channels are coupled, because the hyperfine interaction of the two atom system is

neither diagonal in the total electronic spin  $\hat{S} = \hat{S}_1 + \hat{S}_2$  nor in the total nuclear spin  $\hat{I} = \hat{I}_1 + \hat{I}_2$  [4, 32].<sup>9</sup>

This coupling leads to a coherent superposition of the unbound open channel and the bound closed channel wavefunction during the collision. When the admixture of the bound state is relatively small such that the region of the avoided crossing is large (see Fig. 2.13b), the Feshbach resonance is commonly classified as *broad* or *open-channel dominated*. In turn, when the admixture of the bound state is large, the extend of the avoided crossing is small and the resonance is called *narrow* or *closed-channel dominated*.

Generally, the divergent behavior of the  $s$ -wave scattering length  $a_s$  at a Feshbach resonance can be efficiently parametrized as a function of the magnetic field  $B$  by the expression

$$a_s(B) = a_{\text{BG}} \left( 1 - \frac{\Delta}{B - B_0} \right). \quad (2.95)$$

Here  $B_0$  denotes the position of the resonance and  $\Delta$  the width, that is the distance between  $B_0$  and the magnetic field, at which the scattering length vanishes (see Fig. 2.13b). The background scattering length  $a_{\text{BG}}$  is the scattering length far away from the resonance that is determined by the last bound state or first virtual bound state of the open channel molecular potential.

### 2.3.3 Creation of Molecules

In the proximity of the Feshbach resonance, on the side of large and positive scattering lengths, a dressed bound state develops with a strong admixture of the open channel wavefunction. Two atoms occupying this bound dressed state can be viewed as a molecule that, in the region of the avoided crossing close to the resonance, has the binding energy

$$E_b \approx \frac{\hbar^2}{2\mu a_s^2}, \quad (2.96)$$

which corresponds to a quadratic dependence on  $(B - B_0)$ . The molecules in this region are often called Feshbach molecules and are extremely weakly bound. Their molecular wavefunction extends to a very large size on the order of the scattering length  $a_s$ . When the magnetic field is tuned further below the resonance the dressed molecule asymptotically turns into the purely bound state of the bare closed channel potential. In this regime the binding energy tunes linearly as a function of the magnetic field following  $E_b = \delta\mu \cdot B$ , where  $\delta\mu$  is the difference in the magnetic moment of the open and the closed channel.

---

<sup>9</sup> In ultracold atom experiments typically alkali atoms are used in their ground states with vanishing orbital angular momentum  $\hat{L}$ .

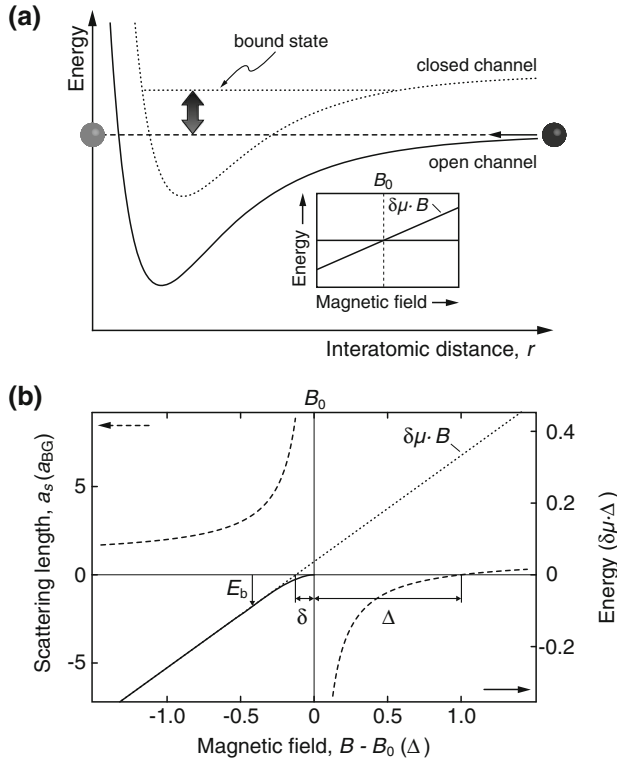


**Fig. 2.13** Feshbach resonance. **a** Two atoms that perform a low energy  $s$ -wave collision in the open channel (solid line) can couple to the bound state of a closed channel potential (dotted line). The bound state can be tuned into resonance using an external magnetic field owing to the different magnetic moments of the open and closed channel spin configurations (inset). **b** The Feshbach resonance gives rise to a divergence of the scattering length  $a_s$  (dashed line). The width  $\Delta$  of the resonance is the distance between the resonance position and the zero crossing of  $a_s$ . The energy of the bare molecular state in the close channel (dotted line) depends linearly on the magnetic field and  $\delta\mu$  is the difference of the magnetic moments in the open and closed channel. The binding energy  $E_b$  of the dressed molecular state (solid line) flattens upon approaching the resonance due to mixing of the open and the closed channel in the region of the avoided crossing. The position of the resonance is shifted by  $\delta$  with respect to the zero crossing of the bare molecular state energy

Feshbach resonances allow to create molecules from free atoms by adiabatically sweeping the magnetic field across the resonance starting from the attractive side [4, 18, 36]. If the Landau-Zener type sweep is performed slowly with respect to the coupling between the open and closed channel and if the temperature of the atomic cloud is low enough, the experimentally achieved conversion efficiencies can reach more than 90 % [37, 38]. Alternatively, the molecular state can be populated using radio-frequency (RF) techniques, which are less efficient, but allow to measure the molecular binding energy [18, 39–41]. In the special case of  $^6\text{Li}$  a cloud of Feshbach

molecules can simply be created by evaporatively cooling the sample on the  $a_s > 0$  side of the resonance [38].

When a Feshbach resonance is used to create molecules of two distinct fermionic species, such as two spin states in  $^6\text{Li}$  or  $^{40}\text{K}$ , it has been observed that the lifetime of the molecules is particularly long close to the resonance position. In this regime, the molecule is well approximated by two individual atoms, such that three-body collisions are strongly suppressed by Pauli's principle prohibiting  $s$ -wave collisions of two identical fermions [42]. Further away from the resonance, the molecule is more closely bound and it becomes less stable against three-body collisions, because here the bosonic character, which favors collisions, tends to dominate over the fermionic quantum statistics of the constituent atoms. Fermionic molecules can be created by using a heteronuclear mixture of fermionic and bosonic species, for example  $^{40}\text{K}$  and  $^{87}\text{Rb}$  or  $^6\text{Li}$  and  $^{23}\text{Na}$  [43]. In contrast to bosonic molecules, those are particularly long-lived far away from the resonance, where close binding lets the molecules clearly show fermionic character and collisions among them are prohibited by Pauli's principle. In turn, close to the resonance the lifetime is expected to be very short. The use of an optical lattice can help to increase the lifetime of Feshbach molecules considerably. Isolating atom pairs on individual lattice sites and transferring them into the molecular state, helps to strongly suppress three-body collisions [39].

Feshbach resonances have become a very important tool in experimental ultracold atom physics. In the context of spin mixtures of interacting fermions, they have enabled the fruitful investigation of the so-called BEC-BCS crossover. The ability to tune the interactions between the spins has dramatic consequences: While for vanishing interactions the two spin states populate independent Fermi seas, they pair up in momentum space for attractive interactions forming a superfluid of Cooper pairs [19, 20]. These pairs in momentum space smoothly connect to the molecular state on the repulsive side of the resonance, where a BEC of molecules forms [44–46]. The superfluidity in the crossover region has been demonstrated by the observation of vortices [21]. Another productive branch of experimental efforts uses Feshbach resonances to create ultracold ground state molecules. Here, the weakly bound Feshbach molecules form the starting point, from which the rovibrational ground state is typically addressed using a STIRAP pulse sequence [47–51].

In the experiments presented of this thesis, the formation of molecules by a Feshbach sweep is used to detect double occupation of lattice sites in an interacting fermionic spin mixture of  $^{40}\text{K}$  atoms (see Chap. 6). Furthermore, RF spectroscopy on KRb molecules has been performed in our experimental setup. These efforts are reported in the PhD thesis of Thorsten Best [52].

### 2.3.4 Two Interacting Atoms in a Harmonic Trap

For the creation of molecules in an optical lattice, it is important to understand the physics of two interacting atoms on an individual lattice site. If the on-site potential is approximated by a harmonic oscillator and the atoms are assumed to interact

through a regularized contact interaction, the problem can be solved analytically [35]. As shown in Fig. 2.14 the energy levels of the bare 3D harmonic oscillator, which correspond to the noninteracting case ( $a_s = 0$ ), get mixed when interactions set in. The contact interaction between the atoms leads to the emergence of a bound state, whose binding energy diverges towards negative infinity at  $a_s = 0$  (see Fig. 2.14a). The application of this level structure to the case of the  $B_0 = 202.1$  G Feshbach resonance of  $^{40}\text{K}$  is shown in Fig. 2.14b. In contrast to the free space situation, the bound molecular state is not entered exactly on resonance, but already at higher magnetic fields starting at  $B_0 + \Delta$ , where the scattering length vanishes [36, 53]. The so-called confinement-induced molecules [39] that exist between  $B_0$  and  $B_0 + \Delta$  dissociate smoothly when the lattice is adiabatically ramped down.

The energy levels of atom pairs on the sites of an optical lattice have been experimentally investigated using RF spectroscopy [39, 40]. Additionally, Fig. 2.14b shows that the first and the second band are smoothly connected, when the magnetic field is ramped from below to above the resonance, which has also been observed experimentally [54].

### 2.3.5 Feshbach Resonances for Rubidium and Potassium

#### The Fermi-Fermi Resonance

In Chap. 6 many-body quantum phases of fermionic spin mixtures in a three-dimensional optical lattice are investigated using  $^{40}\text{K}$  in the hyperfine sublevels  $|F, m_F\rangle = |9/2, -9/2\rangle$  and  $|9/2, -7/2\rangle$ . For this combination of spins a broad (open-channel dominated)  $s$ -wave Feshbach resonance is available at  $B_0 = 202.1$  G to tune interspecies interactions and perform molecule conversion [18, 55–58]. We rely on the parametrization  $a_{\text{BG}} = 174 a_0$  and  $\Delta = 7.8 \pm 0.06$  G given in Ref. [19] (see Fig. 2.15). A recent measurement of the zero crossing of the scattering length in our group suggests an updated width of  $\Delta = 7.0 \pm 0.2$  G [59]. Below the  $s$ -wave resonance, a  $p$ -wave resonance among the  $|9/2, -7/2\rangle$  spins is located at about 199 G [55, 56]. Unfortunately, the presence of this resonance hinders a close approach of the  $s$ -wave resonance on the repulsive side of interactions due to increased losses. The working point at about 175 G corresponds to a scattering length of about  $a_{\text{FF}} = 225 a_0$  and is the strongest repulsion that can safely be addressed for our experimental parameters.

An exemplary molecule conversion and dissociation measurement performed in a harmonically trapped sample is shown in Fig. 2.16. Such measurements allow for a precise determination of the resonance position. Additionally, they can serve as a thermometer as the molecule conversion efficiency has been shown to be a sensitive function of the initial dimensionless temperature  $T/T_F$  of the spin mixture. The conservative value of 80 % conversion efficiency suggests  $T/T_F < 0.15$  according to reference [37].



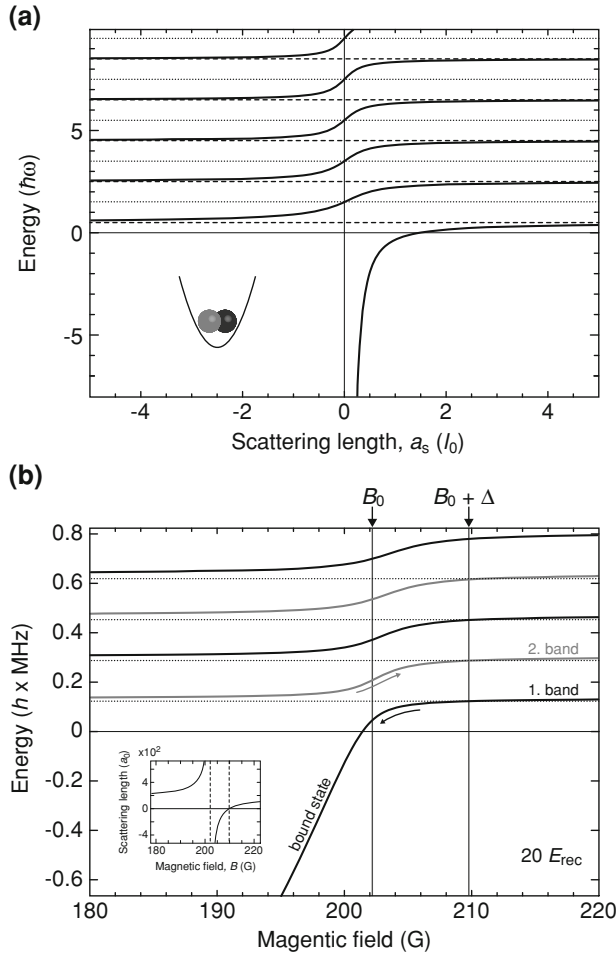


**Fig. 2.14** Two interacting atoms in a harmonic oscillator potential. **a** The general structure of the energy levels obtained in an analytical calculation according to reference [35] is shown as a function of the scattering length  $a_s$  in units of the harmonic oscillator length  $\ell_0 = \sqrt{\hbar/\mu\omega}$ . For vanishing interactions ( $a_s = 0$ ) the energy is given by  $E = \hbar\omega(2n + 3/2)$ , while for infinitely strong attraction or repulsion ( $a_s \rightarrow \pm\infty$ ) the energies are shifted by  $\hbar\omega$  yielding  $E = \hbar\omega(2n + 1/2)$ . **b** Application of the analytical result to a  $^{40}\text{K}$   $|9/2, -9/2\rangle + |9/2, -7/2\rangle$  spin mixture in a  $20 E_{\text{rec}}$  lattice in the vicinity of the Feshbach resonance at  $B_0 = 202.1$  G (see Sect. 2.3.5)

### The Bose-Fermi Resonance

In Chaps. 8 and 9 experiments with interacting Bose-Fermi mixtures are reported. In those investigations we tune the interspecies scattering length with the  $s$ -wave Feshbach resonance at  $B_0 = 546.75(6)$  G between  $^{40}\text{K}$  and  $^{87}\text{Rb}$  in the absolute

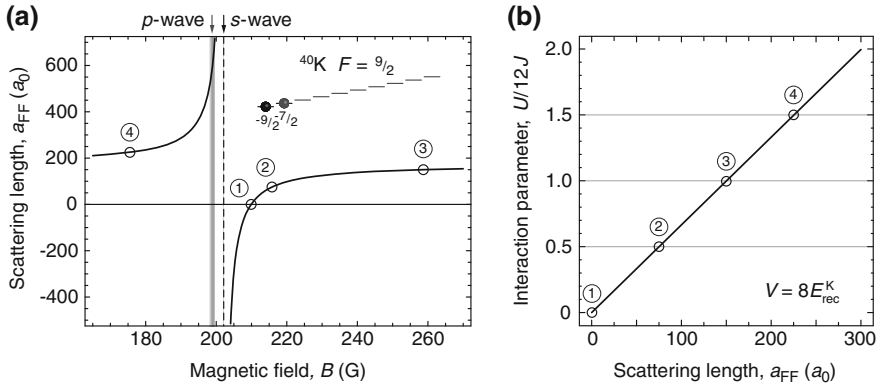


**Fig. 2.15** Tunable fermionic  $^{40}\text{K}$  spin mixture. **a** An  $s$ -wave Feshbach resonance between the hyperfine levels  $|9/2, -9/2\rangle$  and  $|9/2, -7/2\rangle$  is located at  $B_0 = 202.1$  G. Slightly below at  $198.8(5)$  G, there is a  $p$ -wave resonance (gray shaded) of atoms in the  $|9/2, -7/2\rangle$  state [55, 56]. **b** In Chap. 6 we investigate repulsively interacting Fermi-Fermi mixtures in an optical lattice ( $\lambda = 738$  nm) at discrete values of the interaction parameter  $U/12J = 0, 0.5, 1.0$  and  $1.5$ . For the fixed lattice depth of  $V = 8 E_{\text{rec}}$ , these working points correspond to the magnetic fields ① 209.9 G, ② 215.8 G, ③ 258.7 G and ④ 175.5 G

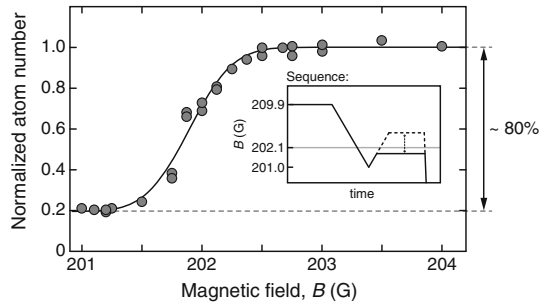
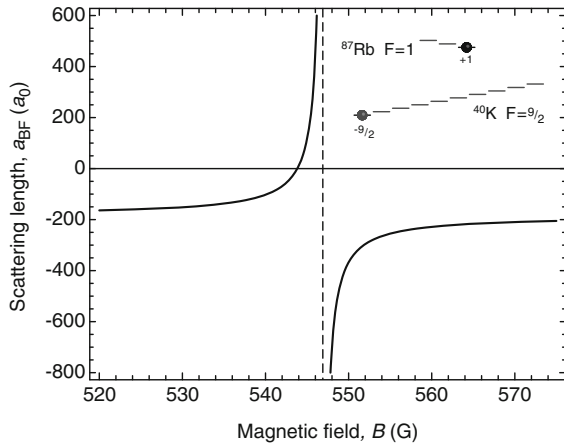


**Fig. 2.16** In a first step, molecules consisting of a  $|9/2, -9/2\rangle$  and a  $|9/2, -7/2\rangle$  atom are created by slowly ramping the magnetic field to  $B = 201$  G below the Feshbach resonance. During time-of-flight expansion the magnetic field is again ramped up and the molecules dissociate when the resonance is crossed (see inset). The number of atoms (normalized to the maximal number of recovered atoms) is shown as a function of the final magnetic field. The solid line is a fit to the data using an error function. The difference of the highest and lowest normalized atom number yields a lower bound to the molecule conversion efficiency, here about 80 %

ground state hyperfine sublevels  $|9/2, -9/2\rangle$  and  $|1, +1\rangle$ , respectively (see Fig. 2.17). The resonance is the most useable of many, mostly extremely narrow ones between  $^{40}\text{K}$  and  $^{87}\text{Rb}$ . It has been characterized in several references [60–64], but the most accurate parametrization has recently been reported by Simoni et al. [65] quoting a background scattering length of  $a_{\text{BG}} = -189 a_0$  and a width of  $\Delta = -3.1$  G.

**Fig. 2.17** Interspecies Feshbach resonance between the absolute ground state hyperfine sublevels  $|9/2, -9/2\rangle$  and  $|1, +1\rangle$  of  $^{40}\text{K}$  and  $^{87}\text{Rb}$ , respectively



Based on the experimental data in Chap. 9, we have been able to precisely extract the magnetic field  $B_0 + \Delta$ , at which the interspecies interactions vanish, confirming the parametrization on a 0.1 G level.

## References

1. K. Huang, *Statistical Mechanics*, 2nd edn. (Wiley, New York, 1987)
2. A. Fetter, J. Walecka, *Quantum Theory of Many-Particle Systems* (Dover Publications, New York, 2003)
3. F. Dalfovo, S. Giorgini, L.P. Pitaevskii, S. Stringari, Theory of Bose-Einstein condensation in trapped gases. *Rev. Mod. Phys.* **71**, 463 (1999)
4. W. Ketterle, M.W. Zwierlein, in *Making, Probing and Understanding Ultracold Fermi Gases*, ed. by M. Inguscio, W. Ketterle, C. Salomon Ultracold Fermi Gases, Proceedings of the International School of Physics “Enrico Fermi”, Course CLXIV, Varenna, 20–30 June 2006, (IOS Press, Amsterdam, 2008)
5. S. Giorgini, L.P. Pitaevskii, S. Stringari, Theory of ultracold atomic Fermi gases. *Rev. Mod. Phys.* **80**, 1215 (2008)
6. W. Zwerger, Mott-Hubbard transition of cold atoms in optical lattices. *J. Opt. B* **5**, S9 (2003)
7. I. Bloch, J. Dalibard, W. Zwerger, Many-body physics with ultracold gases. *Rev. Mod. Phys.* **80**, 885 (2008)
8. W. Pauli, The connection between spin and statistics. *Phys. Rev.* **58**, 716 (1940)
9. L.D. Landau, E.M. Lifshitz, *Quantum Mechanics: Non-relativistic Theory* (Pergamon Press, New York, 1977)
10. L.D. Carr, G.V. Shlyapnikov, Y. Castin, Achieving a BCS transition in an atomic Fermi gas. *Phys. Rev. Lett.* **92**, 150404 (2004)
11. M. Köhl, Thermometry of fermionic atoms in an optical lattice. *Phys. Rev. A* **73**, 031601 (2006)
12. K. Mølmer, Bose condensates and Fermi gases at zero temperature. *Phys. Rev. Lett.* **80**, 1804 (1998)
13. R. Roth, H. Feldmeier, Mean-field instability of trapped dilute boson-fermion mixtures. *Phys. Rev. A* **65**, 021603 (2002)

14. R. Roth, Structure and stability of trapped atomic boson-fermion mixtures. *Phys. Rev. A* **66**, 013614 (2002)
15. C. Ospelkaus, S. Ospelkaus, K. Sengstock, K. Bongs, Interaction-driven dynamics of  $^{40}\text{K}$   $^{87}\text{Rb}$  fermion-boson gas mixtures in the large-particle-number limit. *Phys. Rev. Lett.* **96**, 020401 (2006)
16. D. Jaksch, C. Bruder, J.I. Cirac, C.W. Gardiner, P. Zoller, Cold bosonic atoms in optical lattices. *Phys. Rev. Lett.* **81**, 3108 (1998)
17. M. Greiner, O. Mandel, T. Esslinger, T. Hänsch, I. Bloch, Quantum phase transition from a superfluid to a Mott insulator in a gas of ultracold atoms. *Nature* **415**, 39 (2002)
18. C.A. Regal, C. Ticknor, J.L. Bohn, D.S. Jin, Creation of ultracold molecules from a Fermi gas of atoms. *Nature* **424**, 47 (2003)
19. C.A. Regal, M. Greiner, D.S. Jin, Observation of resonance condensation of fermionic atom pairs. *Phys. Rev. Lett.* **92**, 040403 (2004)
20. M.W. Zwierlein, C.A. Stan, C.H. Schunck, S.M.F. Raupach, A.J. Kerman, W. Ketterle, Condensation of pairs of fermionic atoms near a Feshbach resonance. *Phys. Rev. Lett.* **92**, 120403 (2004)
21. M. Zwierlein, J. Abo-Shaeer, A. Schirotzek, C. Schunck, W. Ketterle, Vortices and superfluidity in a strongly interacting Fermi gas. *Nature* **435**, 1047 (2005)
22. W.D. Phillips, in *Laser Cooling and Trapping of Neutral Atoms*, ed. by W.D. Phillips, E. Arimondo, F. Strumia. Laser Manipulation of Atom and Ions, Proceedings of the International School of Physics “Enrico Fermi” Course CXVIII, (North-Holland, Amsterdam, 1992)
23. O. Morsch, M. Oberthaler, Dynamics of Bose-Einstein condensates in optical lattices. *Rev. Mod. Phys.* **78**, 179 (2006)
24. H. Metcalf, P. van der Straten, *Laser Cooling and Trapping* (Springer, Berlin, 1999)
25. R. Grimm, M. Weidemüller, Y. Ovchinnikov, Optical dipole traps for neutral atoms. *Adv. At. Mol. Opt. Phys.* **42**, 95 (2000)
26. L. Allen, J.H. Eberly, *Optical Resonance and Two-Level Atoms* (Dover Publications, Inc., New York, 1987)
27. C. Cohen-Tannoudji, J. Dupont-Roc, G. Grynberg, *Atom-Photon Interactions* (Wiley, New York, 1998)
28. M. Scully, S. Zubairy, *Quantum Optics* (Cambridge University Press, Cambridge, 1997)
29. R. Loudon, *The Quantum Theory of Light* (Oxford Science Publications), 3rd edn. (OUP, Oxford, 2000)
30. B. Saleh, M. Teich, *Fundamentals of Photonics* (Wiley-Interscience, New York, 1991)
31. N.W. Ashcroft, N.D. Mermin, *Solid State Physics* (Saunders College Publishing, Fort Worth, 1976)
32. C. Chin, R. Grimm, P. Julienne, E. Tiesinga, Feshbach resonances in ultracold gases. *Rev. Mod. Phys.* **82**, 1225 (2010)
33. J.J. Sakurai, *Modern Quantum Mechanics* (Revised edn). (Addison Wesley, Reading, 1994)
34. E.G.M. van Kempen, S.J.J.M.F. Kokkelmans, D.J. Heinzen, B.J. Verhaar, Interisotope determination of ultracold rubidium interactions from three high-precision experiments. *Phys. Rev. Lett.* **88**, 093201 (2002)
35. T. Busch, B.-G. Englert, K. Rzaewski, M. Wilkens, Two cold atoms in a harmonic trap. *Found. Phys.* **28**, 549 (1998)
36. T. Köhler, K. Góral, P.S. Julienne, Production of cold molecules via magnetically tunable Feshbach resonances. *Rev. Mod. Phys.* **78**, 1311 (2006)
37. C. Regal, *Experimental realization of BCS-BEC crossover physics with a Fermi gas of atoms*. Ph.D. Thesis, University of Colorado, 2005
38. M.W. Zwierlein, *High-temperature superfluidity in an ultracold Fermi gas*. Ph.D. Thesis, Massachusetts Institute of Technology, 2006
39. C. Ospelkaus, S. Ospelkaus, L. Humbert, P. Ernst, K. Sengstock, K. Bongs, Ultracold heteronuclear molecules in a 3D optical lattice. *Phys. Rev. Lett.* **97**, 120402 (2006)
40. T. Stöferle, H. Moritz, K. Günter, M. Köhl, T. Esslinger, Molecules of fermionic atoms in an optical lattice. *Phys. Rev. Lett.* **96**, 030401 (2006)

41. C. Klempt, T. Henninger, O. Topic, M. Scherer, L. Kattner, E. Tiemann, W. Ertmer, J.J. Arlt, Radio-frequency association of heteronuclear Feshbach molecules. *Phys. Rev. A* **78**, 061602 (2008)
42. D.S. Petrov, C. Salomon, G.V. Shlyapnikov, Weakly bound dimers of fermionic atoms. *Phys. Rev. Lett.* **93**, 090404 (2004)
43. C.A. Stan, M.W. Zwierlein, C.H. Schunck, S.M.F. Raupach, W. Ketterle, Observation of Feshbach resonances between two different atomic species. *Phys. Rev. Lett.* **93**, 143001 (2004)
44. S. Jochim, M. Bartenstein, A. Altmeyer, G. Hendl, S. Riedl, C. Chin, J. Hecker Denschlag, R. Grimm, Bose-Einstein condensation of molecules. *Science* **302**, 2101 (2003)
45. M. Greiner, C. Regal, D. Jin, Emergence of a molecular Bose-Einstein condensate from a Fermi gas. *Nature* **426**, 537 (2003)
46. M.W. Zwierlein, C.A. Stan, C.H. Schunck, S.M.F. Raupach, S. Gupta, Z. Hadzibabic, W. Ketterle, Observation of Bose-Einstein condensation of molecules. *Phys. Rev. Lett.* **91**, 250401 (2003)
47. S. Ospelkaus, A. Pe'er, K. Ni, J. Zirbel, B. Neyenhuis, S. Kotochigova, P. Julienne, J. Ye, D. Jin, Efficient state transfer in an ultracold dense gas of heteronuclear molecules. *Nat. Phys.* **4**, 622 (2008)
48. K.-K. Ni, S. Ospelkaus, M.H.G. de Miranda, A. Pe'er, B. Neyenhuis, J.J. Zirbel, S. Kotochigova, P.S. Julienne, D.S. Jin, J. Ye, A high phase-space-density gas of polar molecules. *Science* **322**, 231 (2008)
49. J. Danzl, E. Haller, M. Gustavsson, M. Mark, R. Hart, N. Bouloufa, O. Dulieu, H. Ritsch, H.-C. Nägerl, Quantum gas of deeply bound ground state molecules. *Science* **321**, 1062 (2008)
50. J. Danzl, M. Mark, E. Haller, M. Gustavsson, R. Hart, J. Aldegunde, J. Hutson, H.-C. Nägerl, An ultracold high-density sample of rovibronic ground-state molecules in an optical lattice. *Nat. Phys.* **6**, 265 (2010)
51. S. Ospelkaus, K.-K. Ni, D. Wang, M.H.G. de Miranda, B. Neyenhuis, G. Quemener, P.S. Julienne, J.L. Bohn, D.S. Jin, J. Ye, Quantum-state controlled chemical reactions of ultracold potassium-rubidium molecules. *Science* **327**, 853 (2010)
52. T. Best, *Interacting Bose-Fermi mixtures in optical lattices*. Ph.D. Thesis, Universität Mainz, 2011
53. D.B.M. Dickerscheid, U. Al Khawaja, D. van Oosten, H.T.C. Stoof, Feshbach resonances in an optical lattice. *Phys. Rev. A* **71**, 043604 (2005)
54. M. Köhl, H. Moritz, T. Stöferle, K. Günter, T. Esslinger, Fermionic atoms in a three dimensional optical lattice: observing Fermi surfaces, dynamics, and interactions. *Phys. Rev. Lett.* **94**, 080403 (2005)
55. C.A. Regal, C. Ticknor, J.L. Bohn, D.S. Jin, Tuning  $p$ -wave interactions in an ultracold Fermi gas of atoms. *Phys. Rev. Lett.* **90**, 053201 (2003)
56. C. Ticknor, C.A. Regal, D.S. Jin, J.L. Bohn, Multiplet structure of Feshbach resonances in nonzero partial waves. *Phys. Rev. A* **69**, 042712 (2004)
57. T. Loftus, C.A. Regal, C. Ticknor, J.L. Bohn, D.S. Jin, Resonant control of elastic collisions in an optically trapped Fermi gas of atoms. *Phys. Rev. Lett.* **88**, 173201 (2002)
58. C.A. Regal, D.S. Jin, Measurement of positive and negative scattering lengths in a Fermi gas of atoms. *Phys. Rev. Lett.* **90**, 230404 (2003)
59. U. Schneider, L. Hackermüller, J.P. Ronzheimer, S. Will, S. Braun, T. Best, I. Bloch, E. Demler, S. Mandt, D. Rasch, A. Rosch, Fermionic transport and out-of-equilibrium dynamics in a homogeneous Hubbard model with ultracold atoms. *Nat. Phys.* **8**, 213 (2012)
60. K. Günter, T. Stöferle, H. Moritz, M. Köhl, T. Esslinger, Bose-Fermi mixtures in a three-dimensional optical lattice. *Phys. Rev. Lett.* **96**, 180402 (2006)
61. S. Ospelkaus, C. Ospelkaus, O. Wille, M. Succo, P. Ernst, K. Sengstock, K. Bongs, Localization of bosonic atoms by fermionic impurities in a three-dimensional optical lattice. *Phys. Rev. Lett.* **96**, 180403 (2006)
62. M. Zaccanti, C. D'Errico, F. Ferlaino, G. Roati, M. Inguscio, G. Modugno, Control of the interaction in a Fermi-Bose mixture. *Phys. Rev. A* **74**, 041605 (2006)

- 63. F. Ferlaino, C. D'Errico, G. Roati, M. Zaccanti, M. Inguscio, G. Modugno, A. Simoni, Feshbach spectroscopy of a K–Rb atomic mixture. *Phys. Rev. A* **73**, 040702 (2006)
- 64. C. Klempt, T. Henninger, O. Topic, J. Will, W. Ertmer, E. Tiemann, J. Arlt,  $^{40}\text{K}$ - $^{87}\text{Rb}$  Feshbach resonances: modeling the interatomic potential. *Phys. Rev. A* **76**, 020701 (2007)
- 65. A. Simoni, M. Zaccanti, C. D'Errico, M. Fattori, G. Roati, M. Inguscio, G. Modugno, Near-threshold model for ultracold KRb dimers from interisotope Feshbach spectroscopy. *Phys. Rev. A* **77**, 052705 (2008)

<http://www.springer.com/978-3-642-33632-4>

From Atom Optics to Quantum Simulation  
Interacting Bosons and Fermions in Three-Dimensional  
Optical Lattice Potentials

Will, S.

2013, XVIII, 258 p., Hardcover

ISBN: 978-3-642-33632-4